Available online at www.sciencedirect.com

ScienceDirect

Geochimica et Cosmochimica Acta xxx (2021) xxx–xxx

Geochimica et Cosmochimica Acta

www.elsevier.com/locate/gca

Intense biogeochemical iron cycling revealed in Neoarchean micropyrites from stromatolites

Marie-Noëlle Decraene [a,b,*], Johanna Marin-Carbonne [a], Christophe Thomazo [c,d], Nicolas Olivier [e], Pascal Philippot [f,g], Harald Strauss [h], Etienne Deloule [b]

[a] *Institut des Sciences de la Terre, Université de Lausanne, Lausanne, Switzerland*
[b] *Université de Lorraine, CNRS, CRPG, 54500 Vandoeuvre les Nancy, France*
[c] *UMR CNRS 5561 Biogéosciences, Université de Bourgogne Franche Comté, Dijon, France*
[d] *Institut Universitaire de France*
[e] *Université Clermont Auvergne, CNRS, IRD, Laboratoire Magmas et Volcans, F-63000 Clermont-Ferrand, France*
[f] *Géosciences Montpellier, CNRS UMR 5243, Université de Montpellier, 34000 Montpellier, France*
[g] *Institute of Astronomy, Geophysics and Atmospheric Sciences, University of São Paulo, Rua do Matão 1226, Cidade Universitária, 05508-090 São Paulo, Brazil*
[h] *Westfälische Wilhelms-Universität, Institut für Geologie und Paläontologie, Corrensstr, 24, 48149 Münster, Germany*

Received 22 March 2021; accepted in revised form 19 July 2021; available online xxxx

Abstract

Iron isotope compositions of sedimentary pyrites (FeS_2) are used to constrain the redox evolution of the Precambrian ocean and early Fe-based metabolisms such as Dissimilatory Iron Reduction (DIR). Sedimentary pyrites can record biotic and abiotic iron reduction, which have similar ranges of Fe isotopic fractionation, as well as post-depositional histories and metamorphic overprints that can modify Fe isotope compositions. However, some exceptionally well-preserved sedimentary records, such as the stromatolite-bearing Tumbiana Formation (ca. 2.7 Ga, Western Australia) have been proven to retain primary information on Early Neoarchean microbial ecosystems and associated metabolic pathways. Here, we present *in situ* Fe isotope measurements of micropyrites included in four stromatolites from the Tumbiana Formation in order to assess iron respiration metabolism using Fe isotope signatures. A set of 142 micropyrites has been analyzed in three lamina types, *i.e.* micritic, organic-rich and fenestral laminae, by Secondary Ion Mass Spectrometry (SIMS), using a Hyperion radio-frequency plasma source. The diversity of laminae is attributed to specific depositional environments, leading to the formation of Type 1 (micritic laminae) and Type 2 (organic-rich laminae) and early diagenetic effects (Type 3, fenestral laminae). Type 1 and 2 laminae preserved comparable δ^{56}Fe ranges, respectively from −1.76‰ to +4.15‰ and from −1.54‰ to +4.44‰. Type 3 laminae recorded a similar range, although slightly more negative δ^{56}Fe values between −2.20‰ and +2.65‰. Globally, our data show a large range of δ^{56}Fe values, from −2.20‰ to +4.44‰, with a unimodal distribution that differs from the bimodal distribution previously reported in the Tumbiana stromatolites. Such a large range and unimodal distribution cannot be explained by a unique process (*e.g.*, biotic/abiotic Fe reduction or pyrite formation only controlled by the precipitation rate). It rather could reflect a two-step iron cycling process in the sediment pore water including i) partial Fe oxidation forming $Fe(OH)_3$ with positive δ^{56}Fe values followed by ii) partial, possibly microbially induced, Fe reduction leading to Fe^{2+} availability for pyrite formation by sulfate reducers carrying both negative δ^{56}Fe and δ^{34}S signatures. In this model, the buildup and subsequent reduction through time of a residual $Fe(OH)_3$ reservoir arising from the activity of methanotrophs, can explain the strongly positive $\delta^{56}Fe_{Fe(OH)3}$ values up to 4‰. These results indicate that Archean microbial mats have been the site of the

Abbreviations: DIR, Dissimilatory Iron Reduction; MSR, Microbial Sulfate Reduction; AOM, Anaerobic Oxidation of Methane; SEM, Scanning Electron Microscopy; SIMS, Secondary Ion Mass Spectrometry

* Corresponding author at: Institut des Sciences de la Terre, Université de Lausanne, Lausanne, Suisse.
E-mail address: marie-noelle.decraene@unil.ch (M.-N. Decraene).

https://doi.org/10.1016/j.gca.2021.07.020

interaction of several closely linked biogeochemical cycles involving Fe, S and C.

Keywords: Early life; Stromatolites; Tumbiana Formation; Iron isotopes; Ion microprobe; Iron respiration

1. INTRODUCTION

Stromatolites are laminated organo-sedimentary structures, formed by microbial activities in response to environmental and sediment dynamics, and are considered to be the most undisputable evidence of early life on Earth (Allwood et al., 2006; Awramik, 2006; Schopf et al., 2007). The 2.724 Ga old Tumbiana Formation, Western Australia, contains some of the best preserved and most diverse Archean stromatolitic carbonate structures (Buick, 1992; Sakurai et al., 2005; Awramik and Buchheim, 2009; Coffey et al., 2013), including domal, conical, ridged and tufted mm- to m-scale morphologies (Buick, 1992; Flannery and Walter, 2012). A variety of isotopic proxies such as $\delta^{13}C_{org}$, $\delta^{98/95}Mo$ and $\delta^{82/78}Se$ have been interpreted to reflect the buildup of oxidized dissolved species that could result from the activity of oxygenic photosynthetizers (Coffey et al., 2013; Stüeken et al., 2015a; Williford et al., 2016; Stüeken et al., 2017). The record of one of the largest organic carbon isotope excursions on Earth, the Fortescue Excursion, with $\delta^{13}C_{org}$ values as low as −60‰ (Hayes, 1994; Hinrichs, 2002) has been interpreted to represent either the incorporation of ^{12}C in organic matter during oxidation of methane through methanotrophy (Schidlowski, 1982; Hayes, 1994; Eigenbrode and Freeman, 2006; Thomazo et al., 2009; Lepot et al., 2019) or linked to acetogenesis using Acetyl-coA metabolisms (Slotznick and Fischer, 2016), although this latter pathway has been considered unlikely in the Tumbiana stromatolites by other workers (Lepot et al., 2019). Other biological pathways reported in these stromatolites include Microbial Sulfate Reduction (Thomazo et al., 2009; Marin-Carbonne et al., 2018), Dissimilatory Iron Reduction (Yoshiya et al., 2012), arsenic cycling involving both As(III) oxidation and As(V) reduction (Sforna et al., 2014), microbially-induced ammonia oxidation leading to one of the most extreme isotopic ^{15}N enrichment ($\delta^{15}N$ up to +50‰) ever recorded on Earth (Thomazo et al., 2011; Stüeken et al., 2015b), and microbially-derived nano-aragonite precipitates associated with organic globules containing aromatic, aliphatic and carboxyl groups (Lepot et al., 2008; Lepot et al., 2009).

The presence of sulfate and Fe-oxides at the time of deposition and/or early diagenesis may have fueled the reaction of anaerobic oxidation of methane (AOM) in the Tumbiana Formation (Marin-Carbonne et al., 2018; Lepot et al., 2019). Sulfato-reducing metabolizers reduce sulfate into dissolved S species (*e.g.*, H_2S, HS^-, S_0), a process accompanied by a large fractionation of sulfur isotopes between sulfide and sulfate of ~70‰ (*e.g.*, Johnston, 2011; Sim et al., 2011). This metabolic effect has been identified in the Tumbiana Formation by bulk rock (Thomazo et al., 2009) and *in situ* (Marin-Carbonne et al., 2018) S-isotope analyses, although the extent of the measured isotopic fractionation differed from one technique to another. The reduced $\delta^{34}S$ range of ~8‰ measured by bulk analyses has been interpreted as MSR completed under low sulfate concentrations, as expected during the Archean (Crowe et al., 2014). In contrast, the larger $\delta^{34}S$ range of ~84‰ recorded at the lamina scale confirms the activity of MSR associated with locally high sulfate concentrations (Marin-Carbonne et al., 2018). DIR reduces Fe-oxides into dissolved Fe^{2+} and is associated with Fe isotopic fractionation of −2.9‰ between ferrous iron and Fe-oxides (Crosby et al., 2005; Crosby et al., 2007). Although a bulk rock study reported a limited $\delta^{56}Fe$ range in the Tumbiana Formation interpreted to reflect a limited Fe cycle (Czaja et al., 2010), *in situ* laser ablation analyses evidenced a larger Fe isotopic range of both negative and positive $\delta^{56}Fe$ values between −4.2‰ and +2.1‰, interpreted as reflecting an active Fe cycling (Nishizawa et al., 2010; Yoshiya et al., 2012). Ideally, coupled analyses of Fe and S isotopes of pyrites can provide informations on the intimate link between Fe and S cycling in microbial mats (Archer and Vance, 2006; Marin-Carbonne et al., 2014). While $\delta^{34}S$ analyses at the scale of individual microscopic pyrites have been performed in stromatolitic laminae of the Tumbiana Formation (Marin-Carbonne et al., 2018), this approach was not available until recently for Fe isotopes.

Here we use the new procedure developed for micrometric scale analyses of Fe isotopes by SIMS (Decraene et al., 2021) to the same micropyrite-bearing laminae present in Tumbiana stromatolites previously investigated by Marin-Carbonne et al. (2018). Results show that a large range of positive and negative $\delta^{56}Fe$ recorded in these micropyrites is best attributed to an intense oxidative and reductive Fe cycling, parsimoniously interpreted as resulting from DIR activity, coupled with methanotrophy and MSR.

2. MATERIAL AND METHODS

2.1. Geological setting and sample collection for SIMS analyses and Fe speciation

The Tumbiana Formation is a sedimentary succession of about 200 m thick, 680 km wide, with an WNW-ESE extension through the Pilbara Craton (Thorne and Trendall, 2001). The Tumbiana Formation is part of the Neoarchean Fortescue Group (Hamersley Basin, Western Australia) and consists of alternating low-metamorphic grade volcanic and sedimentary rocks deposited during a period of continental extension and rifting (Blake and Barley, 1992; Blake, 1993). It has been subdivided in two main members, the Mingah Member, composed of volcanic tuffs, accretionary lapillis, conglomerates and sandstones, and the Meentheena Member, composed of several horizons of

stromatolitic limestones, sandstones and mudstones (Thorne and Trendall, 2001; Sakurai et al., 2005; Flament et al., 2011; Flannery et al., 2014). U-Pb dating on zircons and volcanic rocks yielded depositional ages between 2724 ± 5 Ma and 2715 ± 6 Ma (Arndt et al., 1991; Blake et al., 2004). The Tumbiana Formation overprinted low-grade metamorphism < 300 °C, allowing the preservation of cell-like organic globules in micrites (Lepot et al., 2008). The depositional environment has been interpreted either as a giant lake system (Buick, 1992; Bolhar and Van Kranendonk, 2007; Awramik and Buchheim, 2009; Coffey et al., 2013; Stüeken et al., 2015b) or a shallow marine setting (Thorne and Trendall, 2001; Sakurai et al., 2005).

Our samples are from the PDP1 drill core of the Pilbara Drilling Project, which intercepts the base of the Maddina basalt, the Meentheena Member and the top of the Mingah Member (Philippot et al., 2009). This drill core has been extensively studied over the past decade for its mineralogy and S, C, N isotopic compositions and represents a unique time capsule in the search for Earth's earliest metabolic activities (Thomazo et al., 2007; Lepot et al., 2008; Lepot et al., 2009; Philippot et al., 2009; Thomazo et al., 2011; Marin-Carbonne et al., 2018; Lepot et al., 2019). This SIMS study focuses on four stromatolites from the Meentheena Member, sampled at 67.8 m (GIS67.8), 68.1 m (GIS68.1), 68.9 m (GIS68.9) and 70.8 m (GIS70.8) depth in stromatolite-rich intervals of the PDP1 drill core (Fig. 1). Samples GIS67.8 and GIS68.9 have been previously investigated for their $C_{organic}$ and S_{pyrite} isotopes compositions of carbonaceous matter and nano-scale sulfides at high spatial resolution (Marin-Carbonne et al., 2018; Lepot et al., 2019). A detailed sample description is further provided in Section 3.1.

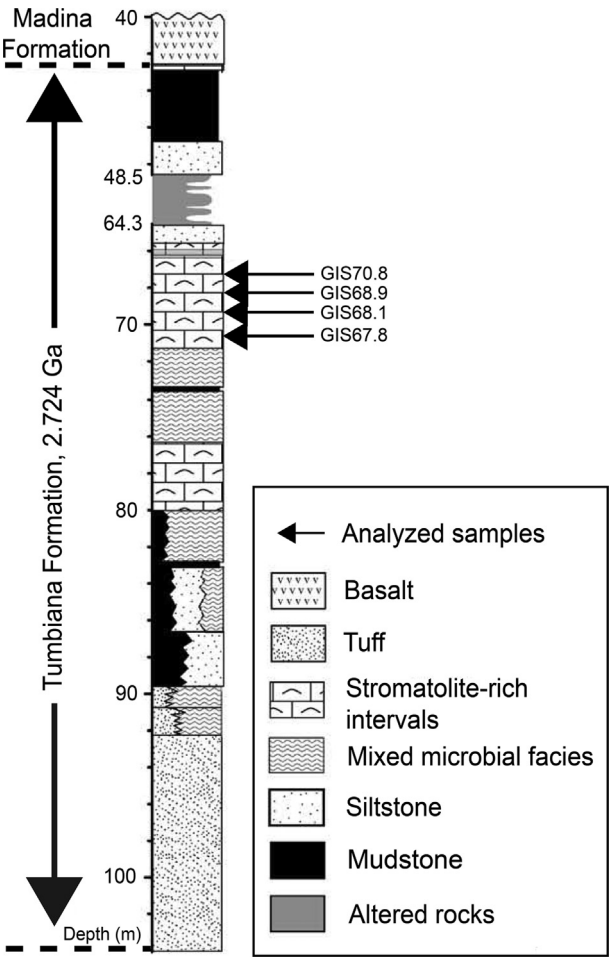

Fig. 1. Simplified log of the PDP1 drill core modified after Thomazo et al. (2009). Black arrows represent the location of the studied samples.

2.2. Optical and SEM observations

The samples were first described by optical microscopy. Scanning Electron Microscopes (SEM) were used at CRPG Nancy (JEOL JSM 6510) and at ISTE Lausanne (Tescan Mira LMU) to produce backscattered electron images at a working distance of 21 mm. Analysis were performed with a 1.5nA primary beam at 20 kV. Energy dispersive X ray spectrometry was used for semi quantitative punctual analysis and mapping to determine elemental composition of the sulfides and to select pyrite rich areas for subsequent SIMS analysis.

2.3. Iron speciation

Identification of Fe-mineral species follows the sequential iron extraction procedure proposed by Poulton and Canfield (2005). Four different mineral phases were extracted: (1) carbonate-associated Fe (Fe_{carb}) present in calcite, siderite and ankerite; (2) Fe contained in oxides, hydroxides and oxyhydroxides (Fe_{ox}) including hematite, goethite, akaganeite, lepidocrocite and ferrihydrite; (3) magnetite (Fe_{mag}) and (4) Fe bound to poorly reactive sheet silicates (Fe_{PRS}) including biotite, chlorite and glauconite. Furthermore, in order to evaluate total iron contents (Fe_T) the technique developed by Aller et al. (1986); see Poulton and Canfield (2005) was applied. Around 200 mg of each sample were ashed (at 450 °C for 8 h) in ceramic crucibles and reacted with 10 mL 6 N HCl. This extraction was conducted at 80 °C for 24 h. Each extracted species of iron described above was reacted with phenantroline and the concentration of the resulting Fe^{2+}-phenantroline complex was measured using a Genesys spectral photometer Series 10 at 515 nm, at the Institut für Geologie und Paläontologie, Westfälische Wilhelms-Universität Münster, Germany, following the method proposed in Reuschel et al. (2012) and described in detail in Sauvage et al. (2013). The concentration of S associated with pyrite (S_{py}) was evaluated using gravimetric quantification after chromium reducible sulfur extraction (Canfield et al., 1986). Iron associated with pyrite (Fe_{py}) was calculated from the S_{py} assuming a stoichiometric ratio. The total iron concentrations (Fe_T) measured during the course of this study using the sequential extraction method were also compared to previous ICPMS measurements reported in Thomazo et al. (2010). The intercalibration between both methods displays a good correlation ($R^2 = 0.97$, Table 1, Electronic Annex (EA); Fig. EA-1).

Please cite this article in press as: Decraene M. -N., et al. Intense biogeochemical iron cycling revealed in Neoarchean micropyrites from stromatolites. *Geochim. Cosmochim. Acta* (2021), https://doi.org/10.1016/j.gca.2021.07.020

Table 1
Iron speciation data for stromatolite samples, from 42.7 m to 85.7 m depth of the drill core PDP1.

Sample	Lithology	Al (ppm)	Fe_T (ppm)	Fe_{ICPMS} (ppm)	Fe_{py} (ppm)	Fe_{carb} (ppm)	Fe_{ox} (ppm)	Fe_{mag} (ppm)	Fe_{PRS} (ppm)	$Fe_U + Fe_{PRS}$ (ppm)	Fe_{HR} (ppm)	Fe_{HR}/Fe_T	Fe_{py}/Fe_{HR}
GIS42.7	Stromatolite	3963.11	10,260.00	11,354	348	3640	178	522	1100	5572.00	4688	0.46	0.07
GIS68.0	Stromatolite	14,257.09	21,443.36	21,707	958	3887	90	316	1194	16,192.36	5251	0.24	0.18
GIS68.2	Stromatolite	22,435.73	*n.a*	25,459	1655	2530	193	464	4109	*n.a*	4842	0.19	0.34
GIS68.9	Stromatolite	55,316.89	*n.a*	42,581	3745	*n.a*	*n.a*	*n.a*	*n.a*	*n.a*	*n.a*	*n.a*	*n.a*
GIS69.2	Stromatolite	17,074.17	26,845.63	27,440	3745	4207	120	826	1104	17,947.63	8898	0.33	0.42
GIS70.4	Stromatolite	15,332.43	18,687.26	18,949	1742	3967	41	312	755	12,625.26	6062	0.32	0.29
GIS70.8	Stromatolite	18,578.64	22,503.36	22,960	87	3642	204	813	1306	17,757.36	4746	0.21	0.02
GIS72.1	Stromatolite	8976.31	12,697.44	12,446	523	2794	12	149	284	9219.44	3478	0.27	0.15
GIS77.1	Stromatolite	4483.11	*n.a*	12,628	1045	3860	324	*n.a*	509	*n.a*	*n.a*	*n.a*	*n.a*
GIS77.2	Stromatolite	51,989.90	*n.a*	57,246	958	1391	325	571	2741	*n.a*	3245	0.06	
GIS78.1	Stromatolite	6275.34	10,370.15	15,330	1132	4018	114	171	510	4935.15	5435	0.52	0.21
GIS78.4	Stromatolite	7123.50	17,622.55	16,177	697	3649	82	371	659	12,823.55	4799	0.27	0.15
GIS83.2	Stromatolite	21,143.30	46,724.23	43,029	958	4765	188	1605	2277	39,208.23	7516	0.16	0.13
GIS85.7	Stromatolite	*n.a*	34,037.77	*n.a*	2003	4947	277	1620	2959	25,190.77	8847	0.26	0.23

Because of their high reactivity toward hydrogen sulfide (Canfield et al., 1992; Poulton and Canfield, 2005), the sum of Fe_{carb}, Fe_{ox}, Fe_{mag} and Fe_{py} are referred to as 'Highly Reactive' Fe fraction (Fe_{HR}) of the total iron. Fe_{HR}/Fe_T ratio is commonly used to scale anoxic conditions when values are above a threshold of 0.38 (Raiswell and Canfield, 1998). Fe_{HR} enrichment, in excess toward this maximal detrital background, indicates an external source of reactive Fe decoupled from the siliciclastic flux. Euxinic conditions can also be recognized when both Fe_{HR}/Fe_T and Fe_{py}/Fe_{HR} exceed thresholds of 0.38 and 0.80, respectively. However, in lacustrine environment, bias due to high sedimentation rates makes threshold based on Fe_{HR}/Fe_T questionable (Lyons and Severmann, 2006) and Tumbiana Fe speciation data should be interpreted with caution.

2.4. *In situ* Fe isotope analyses of micropyrites by SIMS

142 micropyrites were analyzed over three SIMS sessions (April 2018, July 2018 and October 2018). One reference standard grain was included in each sample mount, and the mounts were carbon-coated before analysis. *In situ* iron isotope analyses were performed with the CAMECA ims 1280HR2 equipped with the new Hyperion radiofrequency source at CRPG-IPNT in Nancy (France). Using the procedure detailed in Decraene et al. (2021), this source allows measurement of micrometric targets (less than 20 microns) with a current density 10 times greater than that of a standard duoplasmatron source (Liu et al., 2018). A 3nA Gaussian $^{16}O^-$ primary beam was focused into a 2.5 to 3 µm spot. Typical ^{56}Fe intensities ranged between $1.2x10^7$ and $8.2x10^7$ counts per second. The mass resolution power was set at ~6800 to resolve interferences on $^{54}Fe^+$ ($^{53}CrH^+$) and on $^{56}Fe^+$ ($^{55}MnH^+$). The measurement of ^{52}Cr allow to monitor the $^{54}Cr^+$ isobaric interference on $^{54}Fe^+$ according to the method described in Marin-Carbonne et al. (2011). Simultaneous measurement of ^{52}Cr, ^{54}Fe, ^{56}Fe and ^{57}Fe was performed in multicollection mode with three off-axis Faraday cups and one electron multiplier for ^{52}Cr. Finally, iron isotope compositions are reported as permil variations of $^{56}Fe/^{54}Fe$ ratios measured in the samples normalized to that of the international reference material IRMM-014 as the following:

$$\delta\,^{56}Fe = \left[\frac{\left(\frac{^{56}Fe}{^{54}Fe}\right)_{sample}}{\left(\frac{^{56}Fe}{^{54}Fe}\right)_{IRMM-014}} - 1\right] * 1000$$

Before running analyses, $^{32}S^+$ isotope images were collected via electron multiplier, in order to record the exact location of the micropyrites (Electronic Annex (EA); Fig. EA-2). Afterward, a 90 s presputtering time was applied, followed by data acquisition in multicollection mode for 300 seconds. Backgrounds of the detectors were measured during presputtering and were substracted from each analysis. Balmat and Spain pyrites (respectively $\delta^{56}Fe_{true}$ = -0.40 ± 0.01‰ Whitehouse and Fedo, 2007 and $\delta^{56}Fe_{true}$= +0.52 ± 0.03‰ Decraene et al., 2021) were used as standards to correct the instrumental mass fractionation

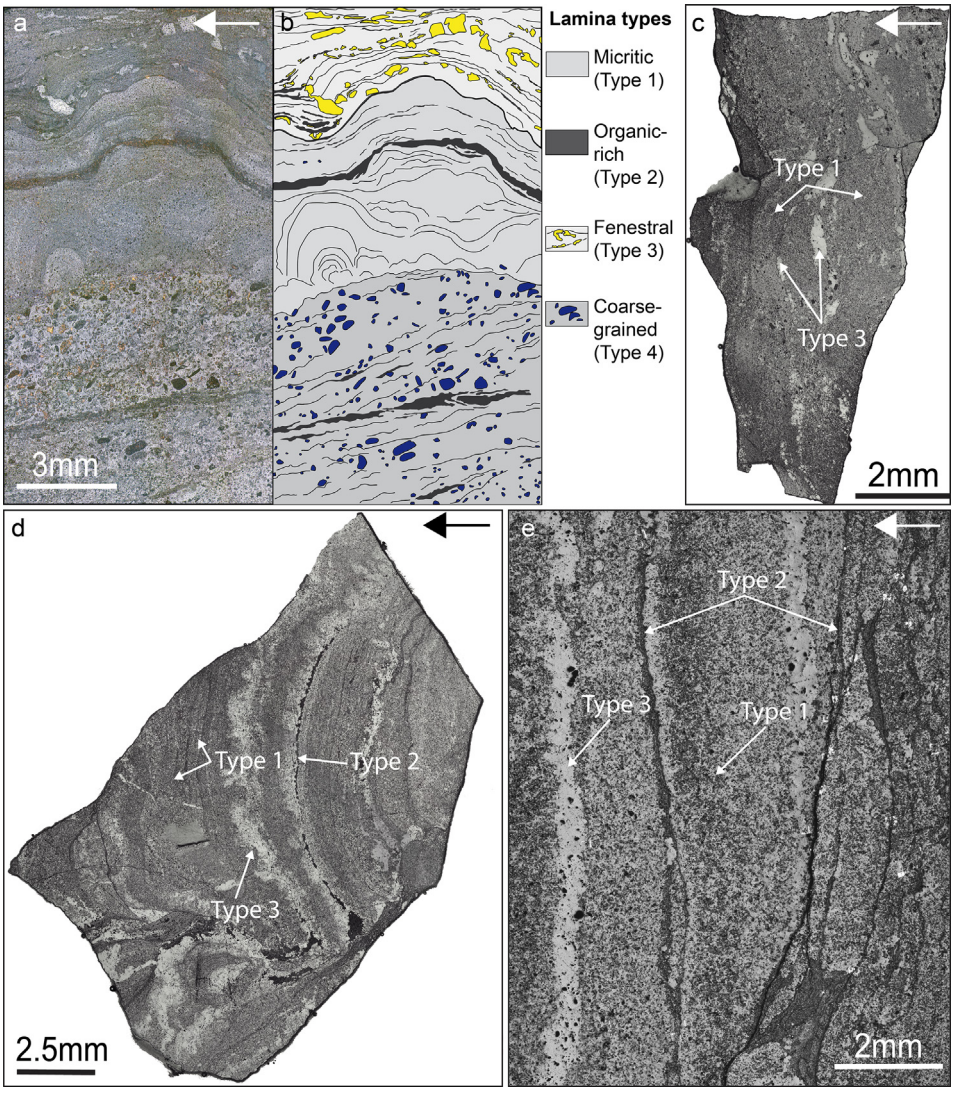

Fig. 2. Optical microscope large views of the four analyzed samples. (a) GIS68.9; (b) Schematic view of the four different laminae (Type 1: Micritic lamina; Type 2: Organic-rich lamina; Type 3: Fenestral lamina and Type 4: coarse-grained lamina) in GIS68.9; (c) GIS70.8; (d) GIS67.8 and (e) GIS68.1. The different types of laminae are indicated by white arrows. The mineralogy of the different laminae is detailed in Fig. 3. Arrows on the top right give the orientation of the samples. (For interpretation of the references to colour in this figure legend, the reader is referred to the web version of this article.)

$\alpha=(^{56}Fe/^{54}Fe)_{meas}/(^{56}Fe/^{54}Fe)_{true}$, defined as the ratio between iron isotopic ratio measured by SIMS and the true ratio determined by MC-ICP-MS (for Multi Collector Inductively Coupled Plasma Mass Spectrometry). The reproducibility was ± 0.24‰ for Balmat pyrite (2SD, standard deviation, April 2018 session; Electronic Annex (EA); Fig. EA-3) and ± 0.28‰ for Spain pyrite (July 2018 session; Electronic Annex (EA); Fig. EA-4; Table EA-1).

3. RESULTS

3.1. Petrographic investigations

The four studied samples are part of a well-developed stromatolite facies and belong to the stromatolite-rich interval described between ~66 to ~71.5 m depth of the PDP1 drill core (Fig. 1, Philippot et al., 2009). The four investigated samples (GIS67.8, GIS68.1, GIS68.9, GIS70.8) show an internal variability in the stromatolite fabric, leading to the recognition of four main types of laminae (Fig. 2):

- Type 1: Micritic laminae, where a cement of micrite represents the major mineral phase, associated with scarce automorphic chlorites and micropyrites. Few micrometric (10 μm to 20 μm) detrital zircons were also observed. This stromatolitic fabric is characterized by well-marked laminated domal structures.
- Type 2: Organic-rich laminae, which are composed of nano to micropyrites and automorphic chlorites. Accessory mineral phases such as sphalerite, zircon and anatase are rare. This type of lamina is often laterally

Please cite this article in press as: Decraene M. -N., et al. Intense biogeochemical iron cycling revealed in Neoarchean micropyrites from stromatolites. *Geochim. Cosmochim. Acta* (2021), https://doi.org/10.1016/j.gca.2021.07.020

discontinuous and is observed between different types of laminae.

- Type 3: Fenestral laminae, which are composed of micritic and sparitic cements, and micropyrites. This laminoid-fenestral fabric is characterized by spar-filled cavities that are arranged along the lamination. These cavities can be either by irregular or elongated horizontal fenestrae, which are embedded in a micritic cement.
- Type 4: coarse-grained laminae, composed of various sedimentary grains such as peloids and ooids, with a sparse and non-continuous internal lamination. These do not contain any pyrite and therefore are not considered in the following geochemical (δ^{56}Fe) comparisons.

Type 1 and 3 laminae have a pluri-millimeter to centimeter thickness whereas Type 2 are sub-millimetric to millimetric. Microcrystalline quartz cement is identified in all samples, independently of the type of laminae, which indicates a post-depositional silicification process (Lepot et al., 2009; Philippot et al., 2009). Pyrites are identified in Type 1, 2 and 3 laminae (Fig. 3) in various proportions (more abundant in organic-rich laminae relative to the others) and exhibit euhedral morphologies, as single grains or aggregates. The size of the pyrites ranges from ~100 nm-20 μm, except for GIS68.1, which present some larger pyrites up to 60 μm. Pyrites associated with organic-rich laminae (Type 2) are mainly between 5 to 10 μm in size and in average ~10 μm in micritic and fenestral laminae (Types 1 and 3). The measured micropyrites have similar size ranges (5 to 15 μm) whatever the lamina type, but the smallest pyrites (<5μm to hundreds nm) are preferentially located in organic-rich (Type 2) laminae (Fig. 3).

3.2. Iron species

Iron speciation was used to evaluate the relative contribution of carbonate, oxide, silicate and sulfide as iron-bearing minerals compared to the total iron content. Iron speciation has been measured in 41 samples from 42.7 m to 90.4 m depth of the PDP1 drill core. Total iron (Fe_T) content in three different lithologies (stromatolites, mudstones and siltstones) vary between 0.64 and 5.69wt.% with a mean value of 2.99wt.%. Results for Fe speciation in the stromatolite facies are shown in Table 1.

Fe_T in stromatolites range between 1.03 and 4.67wt.% with a mean value of 2.22wt.%. Among the different Fe-bearing phases, Fe content was subdivided into three main categories. These include extractable iron (Fe_{ext}) clumped iron in pyrites, oxides, magnetites and carbonates (Fe_{py}, Fe_{ox}, Fe_{mag} and Fe_{carb}); iron in poorly reactive sheet silicates (mainly chlorite, Fe_{PRS}); and unreactive iron (Fe_U), defined as the difference between extractable iron and the total iron contents. The extraction of Fe from poorly reactive sheet silicates is however often incomplete and part of Fe contained in chlorites may participate to the fraction of unreactive iron. Iron oxides display low Fe content between 12 to 325 ppm with an average value of 165 ppm. Fe content in magnetites ranges between 149 to 1620 ppm with an average value of 645 ppm. Except for GIS68.9 and GIS69.2, which display Fe concentrations in pyrites close to 0.37wt.%, the average pyrite Fe content is around 0.10wt.%. Fe content in carbonates varies between 0.14 and 0.49wt.% with a mean value of 0.36wt.%. Fe content associated with poorly reactive silicates displays a range between 0.02 and 0.41wt.%, with an average of 0.15wt.%. We observe that Fe is mostly concentrated in carbonate and in sheet silicates as chlorites. Moreover, the difference between Fe_T and Fe_{ext} shows that a large fraction (~25%) of iron is concentrated in unreactive phases.

3.3. SIMS analyses

3.3.1. Iron isotope compositions

Iron isotope compositions of the 142 micropyrites analyzed in GIS67.8, GIS68.1, GIS68.9 and GIS70.8 are summarized in Table 2. These micropyrites show a large range in iron isotope compositions, between −2.20‰ and +4.44‰ ±0.24‰ (2σ,SD) (Fig. 4a), encompassing the entire terrestrial iron isotope range of values reported in the literature (Dauphas et al., 2017). Stromatolites GIS67.8 and GIS68.9 show a similar large range of δ^{56}Fe between −2.20‰ and +4.15‰ (n = 70) and between −1.44‰ and +4.44‰ (n = 60) respectively, while GIS68.1 and GIS70.8 display mostly positive values and smaller ranges of δ^{56}Fe values from −0.01‰ to +3.79‰ (n = 8) and from +0.49‰ to +2.41‰ (n = 4) respectively (Fig. 4a). In addition, we observe that iron isotope compositions of analyzed micropyrites might be dependent on the

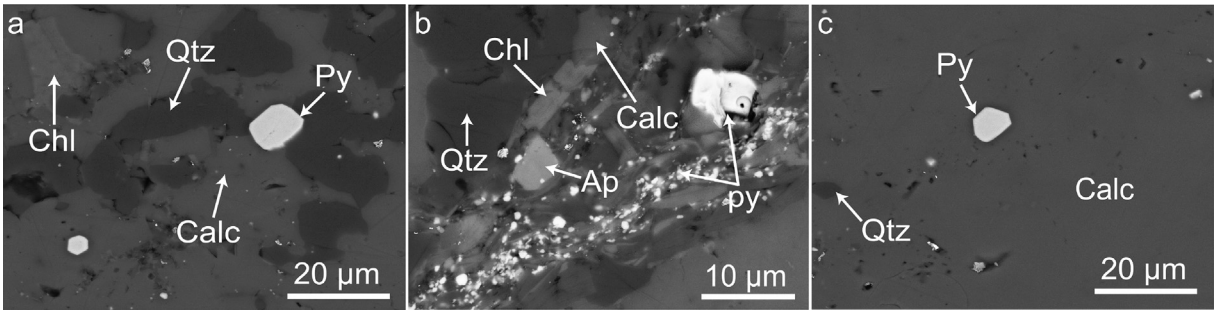

Fig. 3. SEM images of the different types of laminae in which micropyrites were measured. (a) Micropyrites in a micritic lamina (Type 1); (b) Micropyrites in an organic-rich lamina (Type 2); (c) Micropyrites in a fenestra (Type 3). Chl: Chlorite; Qtz: Quartz; Py: Pyrite; Calc: Calcite; Ap: Apatite.

Please cite this article in press as: Decraene M. -N., et al. Intense biogeochemical iron cycling revealed in Neoarchean micropyrites from stromatolites. *Geochim. Cosmochim. Acta* (2021), https://doi.org/10.1016/j.gca.2021.07.020

Table 2
Iron isotope compositions of 142 micropyrites from GIS67.8, GIS68.1, GIS68.9 and GIS70.8 samples of the Tumbiana Formation. The type of lamina refers to micritic laminae (Type 1), organic-rich laminae (Type 2) and fenestral laminae (Type 3).

# Sample	Analyses	$^{56}Fe^{+}$ intensity (cps)	$\delta^{56}Fe$ (‰)	2σ (‰)	Type of lamina
GIS67.8	PDP1-G1Z8a	3.63E+07	−1.86	0.21	3
	PDP1-G1Z16b	1.58E+07	1.39	0.30	3
	PDP1-G1Z14c	7.34E+07	1.13	0.18	2
	PDP1-G1Z13d	8.23E+07	−0.87	0.16	2
	PDP1-G1Z11k	3.37E+07	−0.93	0.19	3
	PDP1-G1Z11j	3.40E+07	−1.17	0.19	3
	PDP1-G1Z11i	3.98E+07	−0.54	0.19	3
	PDP1-G1Z11f	4.40E+07	0.90	0.19	3
	PDP1-G1Z11b	5.60E+07	−0.77	0.16	3
	PDP1-G1-Z33i	3.07E+07	0.81	0.19	1
	PDP1-G1-Z33h	2.15E+07	−0.36	0.22	1
	PDP1-G1-Z33e	2.67E+07	0.53	0.20	1
	PDP1-G1-Z33c	1.50E+07	−0.30	0.32	1
	PDP1-G1-Z33d	1.55E+07	−0.22	0.31	1
	PDP1-G1-Z25e	2.63E+07	2.67	0.23	1
	PDP1-G1-Z33b	2.00E+07	0.52	0.25	1
	PDP1-Z18e	3.51E+07	−0.54	0.21	3
	PDP1-Z19a	4.62E+07	−1.14	0.19	3
	PDP1-Z18b	2.94E+07	−1.00	0.21	3
	PDP1-Z18c	2.75E+07	0.32	0.18	3
	PDP1-Z19b	2.72E+07	−2.20	0.21	3
	PDP1-Z19c	5.68E+07	−0.57	0.16	3
	PDP1-Z19d	2.19E+07	−1.96	0.23	3
	PDP1-Z19e	1.54E+07	1.73	0.34	3
	PDP1-Z19f	4.69E+07	−1.35	0.17	3
	PDP1-Z19g	2.92E+07	2.65	0.22	3
	PDP1-Z20d	3.05E+07	−0.11	0.21	3
	PDP1-Z20e	4.64E+07	−0.81	0.17	3
	PDP1-Z20g	4.77E+07	0.24	0.18	3
	PDP1-Z27a	4.32E+07	−0.54	0.16	2
	PDP1-Z27b	1.45E+07	0.74	0.31	2
	PDP1-Z22a	5.63E+07	0.45	0.17	3
	PDP1-Z31a	2.90E+07	0.09	0.17	2
	PDP1-Z31b	2.39E+07	−0.28	0.26	2
	PDP1-Z31c	5.43E+07	0.63	0.14	2
	PDP1-Z31d	2.34E+07	1.78	0.22	2
	PDP1-Z31e	3.27E+07	−1.54	0.19	2
	PDP1-Z31f	3.59E+07	1.79	0.16	2
	PDP1-Z36a	3.82E+07	−0.38	0.16	2
	PDP1-Z37a	5.87E+07	1.91	0.13	1
	PDP1-Z37b	3.43E+07	0.81	0.22	1
	PDP1_Z1a	2.14E+07	2.36	0.18	1
	PDP1_Z1b	5.49E+07	2.77	0.11	1
	PDP1_Z1c	5.08E+07	1.92	0.14	1
	PDP1_Z1d	2.10E+07	1.37	0.22	1
	PDP1_Z2a	2.67E+07	0.35	0.23	3
	PDP1_Z2b	2.61E+07	0.98	0.18	3
	PDP1_Z2d	2.42E+07	−0.63	0.19	3
	PDP1_Z2e	1.91E+07	0.18	0.26	3
	PDP1_Z2f	5.23E+07	1.54	0.16	3
	PDP1_Z2g	2.94E+07	1.04	0.16	3
	PDP1_Z2h	3.35E+07	1.21	0.14	3
	PDP1-IV-Z9a	2.48E+07	4.15	0.26	1
	PDP1-IV-Z21	2.65E+07	−1.03	0.20	3
	PDP1-IV-Z19a	2.52E+07	−1.27	0.20	3
	PDP1-IV-Z19c	1.76E+07	−0.88	0.24	3
	PDP1-IV-Z19d	1.99E+07	−0.26	0.25	3
	PDP1-IV-Z19e	1.50E+07	2.15	0.33	3
	PDP1-IV-Z19f	1.94E+07	−0.92	0.29	3
	PDP1-IV-Z20	2.68E+07	−0.15	0.22	1

Please cite this article in press as: Decraene M. -N., et al. Intense biogeochemical iron cycling revealed in Neoarchean micropyrites from stromatolites. *Geochim. Cosmochim. Acta* (2021), https://doi.org/10.1016/j.gca.2021.07.020

Table 2 (*continued*)

# Sample	Analyses	$^{56}Fe^{+}$ intensity (cps)	$\delta^{56}Fe$ (‰)	2σ (‰)	Type of lamina
	PDP1-IV-Z18a	3.32E+07	1.17	0.18	3
	PDP1-IV-Z18b	2.11E+07	−2.06	0.25	3
	PDP1-IV-Z12a	3.66E+07	0.84	0.17	1
	PDP1-IV-Z11a	2.46E+07	2.33	0.22	1
	PDP1-IV-Z11b	2.77E+07	−1.40	0.21	1
	PDP1-IV-Z6a	2.09E+07	3.43	0.36	1
	PDP1-IV-Z6b	2.08E+07	0.71	0.23	1
	PDP1-IV-Z4a	2.68E+07	−0.27	0.18	1
	PDP1-IV-Z5a	1.24E+07	−1.76	0.37	1
	PDP1-IV-Z5b	1.54E+07	2.43	0.28	2
GIS68.1	PDP1-III-Z1b	3.49E+07	3.48	0.16	1
	PDP1-III-Z15e	2.70E+07	3.30	0.19	1
	PDP1-III-Z15d	2.41E+07	3.79	0.29	1
	PDP1-III-Z20c	3.62E+07	2.20	0.17	1
	PDP1-III-Z23a	3.42E+07	−0.01	0.20	1
	PDP1-III-Z13a	3.07E+07	0.44	0.17	1
	PDP1-III-Z13b	2.62E+07	1.20	0.18	1
	PDP1-III-Z10b	3.17E+07	2.42	0.23	1
GIS68.9	PDP1-G3Z4a	6.32E+07	−0.21	0.15	1
	PDP1-G3Z4b	4.33E+07	3.81	0.50	1
	PDP1-G3Z4e	5.57E+07	1.34	0.15	1
	PDP1-G3Z4f	6.63E+07	0.81	0.16	1
	PDP1-G3Z4g	3.72E+07	3.41	0.18	1
	PDP1-G3Z4h	6.43E+07	0.10	0.18	1
	PDP1-G3Z4i	5.61E+07	0.45	0.16	1
	TumbianaZ25b	4.62E+07	2.18	0.29	2
	TumbianaZ30a	5.28E+07	−0.33	0.14	1
	TumbianaZ31a	5.98E+07	−0.58	0.16	1
	TumbianaZ31b	6.30E+07	0.17	0.15	1
	TumbianaZ17a	7.06E+07	−0.75	0.14	1
	TumbianaZ17b	7.10E+07	0.07	0.13	1
	TumbianaZ18a	7.65E+07	−1.44	0.13	1
	TumbianaZ16a	7.35E+07	−0.68	0.12	1
	Tumbiana-Z19	7.37E+07	0.45	0.14	1
	Tumbiana-Z15	7.99E+07	−0.36	0.15	1
	Tumbiana-Z23a	2.92E+07	0.02	0.17	2
	Tumbiana-Z23b	6.56E+07	−0.27	0.15	2
	Tumbiana-Z23c	1.86E+07	−1.12	0.45	2
	Tumbiana-Z23f	5.37E+07	1.73	0.17	2
	Tumbiana-Z24b	5.11E+07	2.23	0.24	2
	LE_Z1	6.48E+07	0.91	0.15	2
	LE-Z2e	5.89E+07	4.44	0.16	2
	LE-Z2c	4.42E+07	3.80	0.21	2
	LE-Z4b	5.47E+07	4.02	0.22	2
	LE-Z4a	5.50E+07	0.08	0.17	2
	LE-Z8a	5.72E+07	2.09	0.23	2
	LE-Z12b	5.97E+07	1.42	0.15	2
	LE-Z12a	4.77E+07	2.80	0.17	2
	LE-Z13b	3.20E+07	3.62	0.21	2
	L1_Z2a	4.68E+07	2.05	0.20	2
	L3_Z3	5.48E+07	1.59	0.16	2
	Matrix_Z1b	2.78E+07	1.94	0.19	1
	Matrix_Z1c	5.06E+07	3.06	0.13	1
	Matrix_Z1f	4.73E+07	1.92	0.14	1
	Matrix_Z1e	4.77E+07	3.34	0.15	1
	Matrix_Z1d	5.39E+07	0.55	0.15	1
	Matrix_Z2a	4.60E+07	1.75	0.16	1
	Matrix_Z2b	3.64E+07	1.33	0.15	1
	Matrix_Z2c	2.72E+07	1.65	0.17	1
	Matrix_Z2d	3.03E+07	1.87	0.19	1
	Matrix_Z2e	3.86E+07	0.19	0.14	1
	Matrix_Z3a	4.57E+07	1.02	0.12	1

Please cite this article in press as: Decraene M. -N., et al. Intense biogeochemical iron cycling revealed in Neoarchean micropyrites from stromatolites. *Geochim. Cosmochim. Acta* (2021), https://doi.org/10.1016/j.gca.2021.07.020

Table 2 (*continued*)

# Sample	Analyses	$^{56}Fe^{+}$ intensity (cps)	$\delta^{56}Fe$ (‰)	2σ (‰)	Type of lamina
	Matrix_Z3d	1.68E+07	−1.34	0.27	1
	Matrix_Z3e	4.05E+07	0.78	0.14	1
	Matrix_Z3f	2.78E+07	2.93	0.24	1
	Matrix_Z3g	5.56E+07	1.06	0.13	1
	Matrix_Z3h	4.39E+07	1.25	0.13	1
	Matrix_Z3i	2.21E+07	1.27	0.24	1
	Matrix_Z4a	3.46E+07	1.08	0.18	1
	Matrix_Z4b	1.95E+07	−0.61	0.23	1
	Matrix_Z4c	3.41E+07	1.36	0.15	1
	Matrix_Z4d	4.71E+07	0.45	0.12	1
	Matrix_Z5a	6.67E+07	0.41	0.11	1
	Matrix_Z5b	4.64E+07	1.34	0.13	1
	Matrix_Z5c	3.42E+07	1.09	0.18	1
	Matrix_Z5d	2.98E+07	1.01	0.18	1
	Matrix_Z6b	5.75E+07	0.72	0.12	1
	Matrix_Z6c	5.81E+07	0.96	0.12	1
GIS70.8	PDP1-G2-Z9a	4.28E+07	2.04	0.29	1
	PDP1-G2-Z9b	5.60E+07	0.49	0.14	1
	PDP1-G2-Z9d	5.24E+07	1.72	0.15	1
	PDP1-G2-Z9e	5.69E+07	2.41	0.15	1

type of their hosting lamina (Fig. 4b). Pyrites measured in micritic laminae show large isotopic variations ($\delta^{56}Fe$ from −1.76‰ to +4.15‰, n = 77), comparable with those recorded in pyrites hosted in organic-rich laminae ($\delta^{56}Fe$ from −1.54‰ to +4.44‰, n = 29). In comparison, fenestral laminae yield a smaller Fe isotope signal from −2.20‰ to +2.65‰ (n = 36). The median $\delta^{56}Fe$ value is +1.01‰ in micritic type laminae, +1.42‰ in organic-rich laminae and −0.54‰ in fenestral laminae (Fig. 4c).

Iron isotopic compositions can also be correlated with the pyrite sizes (Fig. 5). Fe isotopic compositions range between −0.54‰ and +2.67‰ for pyrites below 5 μm in size (n = 9, mean $\delta^{56}Fe$ = 0.69‰), between −1.76‰ and +3.94‰ for the 5–10 μm category (n = 64, mean $\delta^{56}Fe$ = 0.68‰), −2.20‰ and +4.44‰ for pyrites of [10–15] μm (n = 53, mean $\delta^{56}Fe$ = 0.92‰) and between −1.44‰ and +3.48‰ for pyrites bigger than 15 μm (n = 16, mean $\delta^{56}Fe$ = 1.07‰). Pyrites > 10 μm in size seem to record ^{56}Fe-enriched isotopic compositions. However, due to the difference in the population size of each categories, we cannot conclude on a clear influence of the size of the pyrites on their respective Fe isotopic compositions. Furthermore, pyrites with similar size can record a large Fe isotopic range (Fig. 6a and b; pyrites of 8–9 μm size have $\delta^{56}Fe$ values between −0.61‰ and +4.02‰). Finally, individual pyrite grain observations after SIMS analysis support that there is no correlation between the $\delta^{56}Fe$ values and the pyrite shapes (Fig. 6c; Electronic Annex (EA); Fig. EA-5).

3.3.2. Probability density and comparison with previous in situ studies

Iron isotopic compositions are presented using probability densities, which calculate a Gaussian function for each analysis considering the associated error (Marin-Carbonne et al., 2012). Because probability density distribution strongly depends on bin size and bin boundary, we chose a bin size of 0.1 in order to reduce the bin boundary effects, *i.e.* the distribution has the same shape whatever the starting $\delta^{56}Fe$ value of the probability density, even if artificial secondary peaks are produced (Fig. 7a). We also report cumulative functions which allow us to clearly identify bimodal and modal distributions (Fig. 7). In previous works from the Redmont area, Nishizawa et al. (2010) and Yoshiya et al. (2012) reported a bimodal distribution (Fig. 7b) with a positive mode around +1‰ and a negative mode around −1.8‰. In this study we observe a monomodal $\delta^{56}Fe$ distribution with mode around +1‰ (Fig. 7a). The cumulative probability functions provide an alternative dataset representation (Fig. 7c and d) and show a stair shape distribution, which highlights the two modes observed in the previous studies (Fig. 7d). In this study, probability density and cumulative functions are in good agreement with a theoretical gaussian curve, showing a progressive increasing ramp for the cumulative representation (Fig. 7c). The whole dataset thus follows a gaussian distribution centered at +1‰ (Fig. 7a). The difference between our distribution and previously published distributions is likely due to different grade of metasomatism that affected variously the Redmont and Meentheena localities (White et al., 2014). Moreover, most of the pyrite grains in this study range from 5 to 10 μm when pyrites previously measured by Nishizawa et al. (2010) and Yoshiya et al. (2012) were tens to hundreds of μm. Micropyrites from this study likely recorded more discreet processes that are not evident in larger pyrite grains from the Redmont locality.

Please cite this article in press as: Decraene M. -N., et al. Intense biogeochemical iron cycling revealed in Neoarchean micropyrites from stromatolites. *Geochim. Cosmochim. Acta* (2021), https://doi.org/10.1016/j.gca.2021.07.020

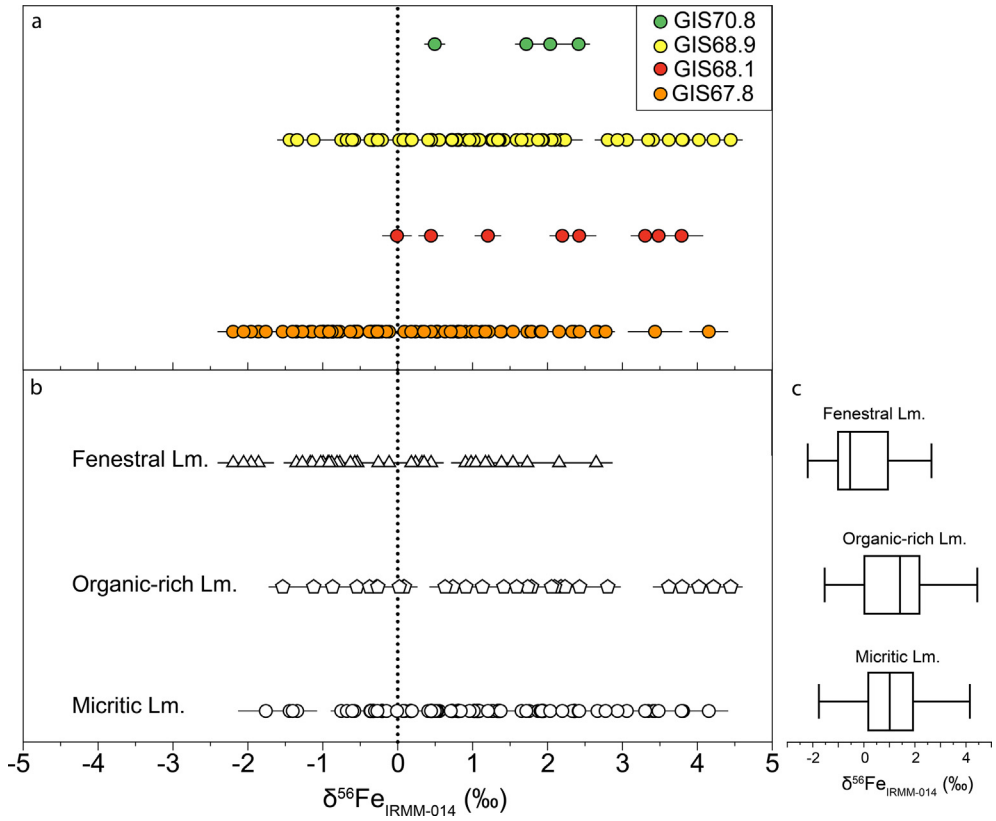

Fig. 4. Iron isotopic compositions measured (a) in the different samples GIS67.8 (orange dots, n = 70), GIS68.1 (red dots, n = 8), GIS68.9 (yellow dots, n = 60) and GIS70.8 (green dots, n = 4); (b) in the different laminae: micritic (Type 1, n = 77), organic-rich (Type 2, n = 29) and fenestrae (Type 3, n = 36). GIS67.8 displays large δ^{56}Fe isotopic range between −2.20‰ and +4.15‰, similar to GIS68.9 isotopic range. Amplitude of isotopic ranges for GIS68.1 and GIS70.8 are less wide and probably un-representative of the whole isotopic variability. In general, more ^{56}Fe-depleted values are observed in fenestrae whereas organic-rich laminae are characterized by ^{56}Fe-enriched isotopic values. Error bars yield the 2SE (standard error); (c) Box plots using δ^{56}Fe values of the different laminae types. (For interpretation of the references to colour in this figure legend, the reader is referred to the web version of this article.)

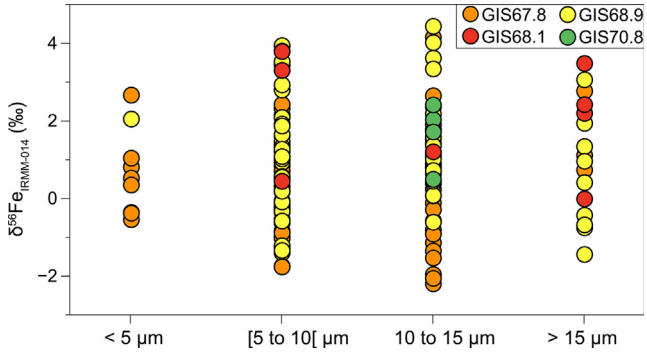

Fig. 5. Iron isotopic compositions as a function of the size of micropyrites. We considered 4 categories of size: less than 5 µm, 5 µm to 10 µm, 10 µm to 15 µm and > 15 µm. (For interpretation of the references to colour in this figure legend, the reader is referred to the web version of this article.)

4. DISCUSSION

The large range of δ^{56}Fe values measured in micropyrites of the Tumbiana Formation could reflect several biotic or abiotic processes. In the following section, we discuss the possible iron sources involved in pyrite precipitation and processes able to explain the range of δ^{56}Fe value recorded in the studied stromatolitic laminae.

4.1. Context of micropyrites precipitation

4.1.1. Pyrite as a minor sink of iron in Tumbiana stromatolites

Although iron speciation proxy is not calibrated for lacustrine environment, important features can be drawn from these analyses. In Tumbiana stromatolites, Fe speciation data show that Fe_{PRS} and Fe_U, mostly represented by

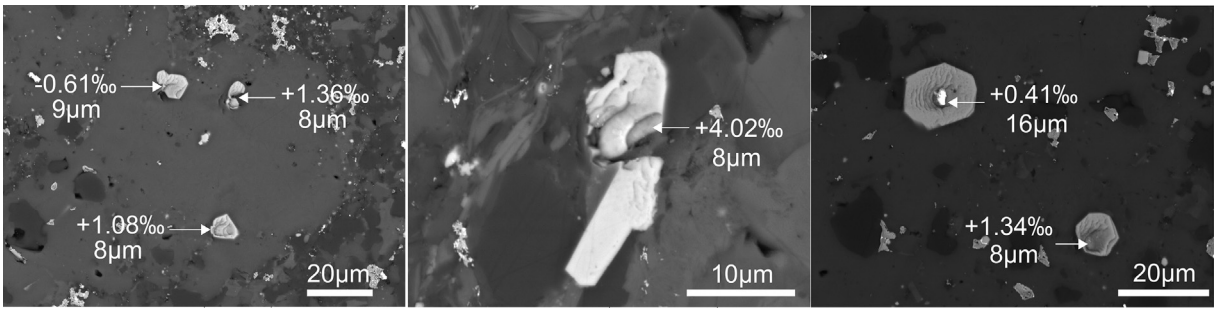

Fig. 6. SEM pictures of micropyrites in GIS68.9. (a) and (b) Fe isotopic compositions measured in pyrites of 8 to 9 µm size. This size category shows an isotopic range up to 4‰, showing the absence of correlation between δ^{56}Fe and the size of the pyrite; c) Fe isotopic compositions of two hexagonal pyrites of 16 µm and 8 µm in size. These pyrites recorded an isotopic difference of 1‰, located at 30 µm from each other, meaning that iron isotopic compositions are not controlled by the shape of the pyrite.

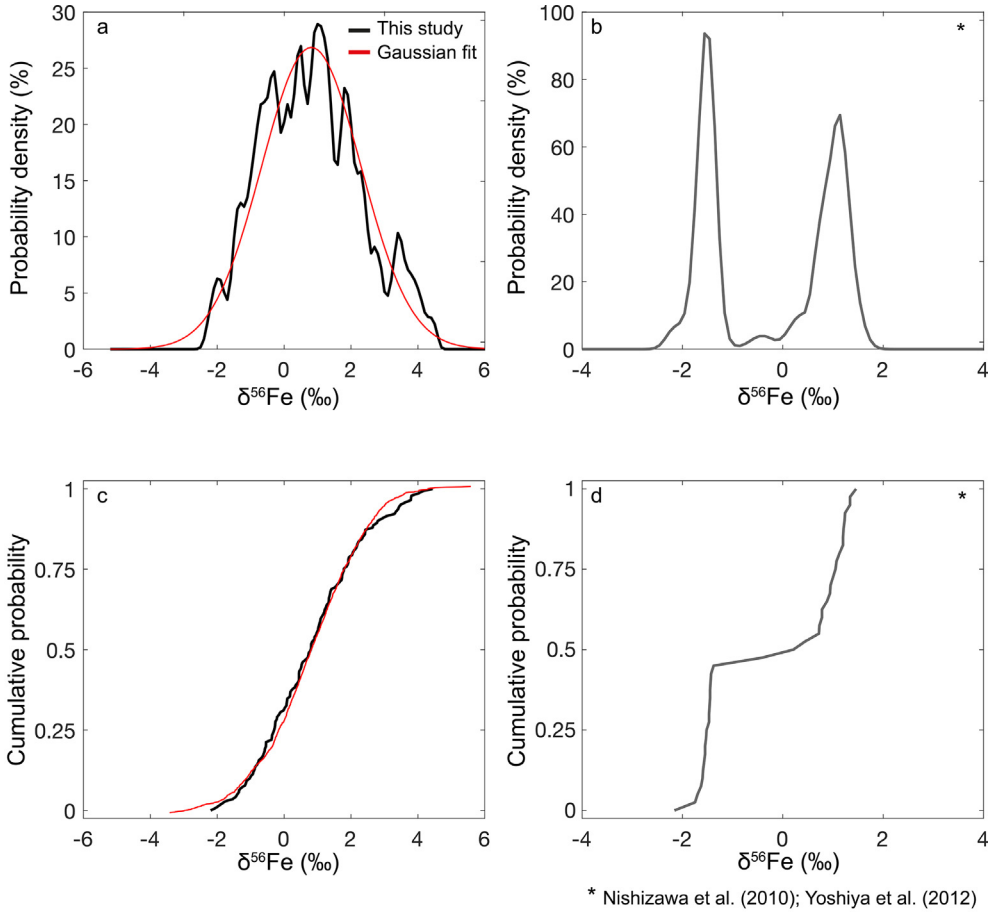

Fig. 7. Probability density distributions calculated for a) the entire δ^{56}Fe dataset (black curve, this study) showing a continuous, gaussian shape distribution centered on +1‰. The red curve represents the theoretical Gaussian function given by $f(x) = \frac{1}{\sigma * \sqrt{2\pi}} * e^{\frac{-(x-\mu)^2}{2\sigma^2}}$ with µ the dataset mean value and σ the standard deviation; b) Previous published δ^{56}Fe values for stromatolite samples describing a bimodal distribution (grey curve, data from Nishizawa et al., 2010; Yoshiya et al., 2012); c) Cumulative function of the entire dataset (black curve, this study) and Gaussian fit (red curve) and d) Cumulative function associated with Nishizawa et al. (2010) and Yoshiya et al. (2012) data. (For interpretation of the references to colour in this figure legend, the reader is referred to the web version of this article.)

chlorites, represent in average 73% of the total iron content (Fe_T). The occurrence of few detrital minerals like zircon and anatase suggests that continental weathering and riverine transport were active during deposition of the Tumbiana sediments. Moreover, in situ weathering and devitrification of the mafic substrate, including volcanic ashes, likely drove the formation of chlorites that are abundant in the samples. As aluminium is a conservative element during weathering and is not remobilized by low temperature hydrothermal fluids, the positive correlation between

Please cite this article in press as: Decraene M. -N., et al. Intense biogeochemical iron cycling revealed in Neoarchean micropyrites from stromatolites. *Geochim. Cosmochim. Acta* (2021), https://doi.org/10.1016/j.gca.2021.07.020

Fe_T and Al contents within stromatolite layers (Electronic Annex (EA); Fig. EA-6) suggests that Fe is mostly inherited from Fe-rich mafic lithologies (Sugisaki, 1978; Wintsch and Kvale, 1994; Sugitani et al., 1996). The input of Fe-rich detritus can explain the low abundance of highly reactive iron (Fe_{HR}) compare to Fe_T (Table 1). The low pyrite content (4% relative to Fe_T) coupled with low Fe_{pyr}/Fe_{HR} ratio (~0.11 on average) argue for non-sulfidic conditions in the Tumbiana water column. However, as organic-matter is sulfidized in the Tumbiana stromatolites (Lepot et al., 2009), variable local sulfidic conditions could have occurred in the sediment pore water. Finally, the micropyrites studied here only reflect a small fraction of the Fe budget in the Tumbiana environment and therefore cannot be considered to account for the whole Tumbiana basin Fe cycling.

4.1.2. Origin of the laminae diversity

The observed fabric variability in our samples underlines the existence of four different types of laminae reflecting diverse mineralization processes leading to the formation of stromatolites (Fig. 2a). The micritic laminae (Type 1), which are mainly made of microcrystalline calcite, reflect a microbial cement precipitation commonly observed in stromatolites through Earth history (Visscher et al., 1998). The organic-rich laminae (Type 2) are chlorite-rich suggesting a terrigenous input in the system. The spatial distribution of these laminae along the domal structure of the stromatolite, their morphology and the lateral variability in thickness argue against a stylolitic origin. Process of trapping of detrital material is highlighted and illustrated by the presence of chlorite, zircon and anatase. The formation of organic matter is associated with the activity of microbial mats. Fenestral laminae (Type 3) are laterally more or less continuous. These sparitic fenestrae indicate a syngenetic or early diagenetic filling of a primary porosity that can be formed by gas released after organic matter or mat breakdown (Tebbutt et al., 1965; Choquette and Pray, 1970; Mata et al., 2012). Finally, the coarse-grained laminae (Type 4), that are devoid of pyrite, highlight an intense trapping and binding of peloids and ooids from adjacent sedimentary bodies. The depositional model of Awramik and Buchheim (2009) for the Meentheena Member positioned the studied stromatolites between shallow and high-energy ooidal grainstones and deeper siltstones and shales. In such a depositional environment, micritic laminae (Type 1) reflect optimal conditions for stromatolite development associated with increased carbonate precipitation. However, the thickness of these micritic laminae does not exceed few millimeters, indicating that their growth was frequently disrupted. Indeed, the Meentheena sedimentary system was relatively dynamic, notably disturbed by rapid lateral facies changes due to frequent storm events (Awramik and Buchheim, 2009). Stromatolite growth was thereby interrupted by recurrent ooidal sand body migration leading to the formation of the coarse-grained laminae (Type 4), or by periods of increased terrigenous runoff to form organic-rich laminae (Type 2). The presence of nutrients associated with river discharges is also consistent with higher rates of organic matter production recorded in these Type 2 laminae. The presence of chlorites also promoted a best post-deposit preservation of organic compounds in this lamina type (Jardine et al., 1989).

Differences in stromatolite growth rates are generally assumed to be controlled by an interplay between internal (microbial communities) and external (*i.e.* environmental) factors (Reid et al., 2000; Dupraz et al., 2009; Bowlin et al., 2012; Bouton et al., 2016). Intrinsic parameters relate to the metabolic activities in the microbial mat or the biofilm, that is the dynamism and diversity of the microbial community. These parameters strongly act on the mineralization of laminae by controlling the availability of HCO^{3-} (the alkalinity) and Ca^{2+} ions (Aloisi, 2008; Dupraz et al., 2009). Extrinsic factors relate to variations in environmental factors, which can influence both the microbial activity and ions availability. These variables include for example, temperature, chemical composition of water (*e.g.*, salinity, pH, alkalinity), solar irradiance, supply (*i.e.* source material and flux) of sedimentary material (Reid et al., 2000; Arp et al., 2003; Andres and Pamela Reid, 2006; Planavsky and Grey, 2008; Jahnert et al., 2013; Bouton et al., 2016; Bouton et al., 2020). Among the different factors that can influence the stromatolite growth and the microbial mineralization potential, physical parameters such as trapping and binding also directly influence stromatolite growth and carbonate precipitation rates (Awramik et al., 1976; Reid et al., 2000; Awramik and Grey, 2005). The diversity of laminae recorded in the Tumbiana stromatolites is a clear illustration of the different processes (mineralization, trapping, terrigenous influence) that can be involved in stromatolite fabric and growth. It also illustrates how the depositional environment and early diagenesis may have influenced the micropyrite distribution and Fe isotopic compositions.

4.1.3. A synsedimentary origin of the micropyrites

In the four analyzed samples, the absence of rounded grains argues against a detrital origin of the pyrites. Similarly, the absence of hydrothermal veins and secondary veins of pyrites argue against a late stage hydrothermal overprint. A limited metamorphic imprint is further supported by $\delta^{13}C$ analyses in carbonate and organic matter, where the range of equilibrium fractionation ($\Delta^{13}C_{carb\text{-}org}$) expected for an isotopic re-equilibration during high-grade metamorphism is inconsistent with the one determined in the Tumbiana samples (Thomazo et al., 2009). The absence of major secondary overprint and preservation of primary features have been likely favored by the pervasive silicification affecting the different samples studied here. Petrographic investigations show that the size, morphology and distribution of the pyrites recorded in the different laminae cannot be used to identify a relative chronology of formation. The smallest pyrites (<5μm to hundreds nm) occur preferentially in intimate association with organic matter in Type 2 laminae and are more concentrated in this lamina type (Fig. 3; Electronic Annex (EA); Fig. EA-7). This indicates a causal relationship between organic matter availability on the abundance of pyrite formed (Rickard et al., 2017). Because micropyrites are enclosed in subparallel stromatolitic laminae, associated with pristine organic matter (Lepot et al., 2009; Marin-Carbonne et al., 2018), and

Please cite this article in press as: Decraene M. -N., et al. Intense biogeochemical iron cycling revealed in Neoarchean micropyrites from stromatolites. *Geochim. Cosmochim. Acta* (2021), https://doi.org/10.1016/j.gca.2021.07.020

display a unimodal Fe isotopic distribution, we interpreted these micropyrites to be precipitated during stromatolite growth or during early diagenesis.

4.2. Large δ^{56}Fe range of micropyrites reflects a kinetic effect

Different processes can account for the large Fe isotope range of values recorded in the studied micropyrites. These include: i) δ^{56}Fe values inherited from Fe sources, ii) Rayleigh distillation process during precipitation of pyrites from monosulfides, iii) variable pyrite precipitation rate (Mansor and Fantle, 2019), iv) H_2S reduction of Fe(III)-oxides and v) Dissimilatory Iron Reduction (DIR) (Yoshiya et al., 2012). All Fe isotope fractionations considered in the following discussion are summarized in Fig. 8.

4.2.1. Iron isotope compositions inherited from Fe sources

Iron isotope compositions of sedimentary micropyrites could be inherited from various sources of Fe to the system. Fe^{2+} may have been delivered from mafic mineral dissolution, the incorporation into authigenic carbonates or magmatic magnetites. Fe isotope fractionation in magmatic rocks are partially attributed to magma evolution processes, such as fractional crystallization or fluid exsolution. The largest range of Fe isotope compositions of ~1.6‰ has been measured in olivine and assigned to Fe-Mg exchange diffusion between olivine and melt (Teng et al., 2011). Except this large isotope range, small fractionations in the order of 0.1‰ to 0.3‰ are typical for magmatic processes (Dauphas et al., 2017 for a review). For example, an equilibrium fractionation of +0.2 ± 0.016‰ has been described between fayalite and magnetite at temperatures ranging between 600 and 800 °C (Shahar et al., 2008). Furthermore, several studies have assessed Fe isotope fractionations that occur during abiotic mafic rock and mineral dissolution. A large Fe isotope fractionation of ~−1.5‰ has been measured for the weathering of a tholeiitic basalt between aqueous Fe released after few hours of experiment and the basalt. Nonetheless, the extend of this fractionation tends to decrease ($\Delta^{56}Fe_{solution\text{-}rock}$ = -0.5‰) as a function of leaching time (Chapman et al., 2009). Only few studies have investigated Fe isotope fractionation during dissolution of silicates. The dissolution of hornblende in the presence of different organic ligands produces dissolved iron slightly enriched in light isotopes, with a maximum fractionation of −0.6‰ between Fe in solution and the mineral (Brantley et al., 2001; Brantley et al., 2004). Similar fractionations were determined during the dissolution of biotite and chlorite from granite (Kiczka et al., 2010). Experiments measuring Fe isotope fractionations between aqueous Fe and siderite have shown $\Delta^{56}Fe_{Fe(II)aq\text{-}siderite}$ of 0‰ and +0.5‰, respectively under biotic and abiotic influences (Wiesli et al., 2004; Johnson et al., 2005). An equilibrium Fe fractionation factor of +0.9‰ has been reported for ankerite formation during microbial DIR (Johnson et al., 2005). Finally, Sossi et al. (2012) reported Fe isotope fractionation of ~+0.1‰ between magnetite and melt at temperature of 900–1000 °C. Thus the Fe isotope range inherited from magmatic processes and/or mineral mineral precipitation is limited and it seems difficult to explain

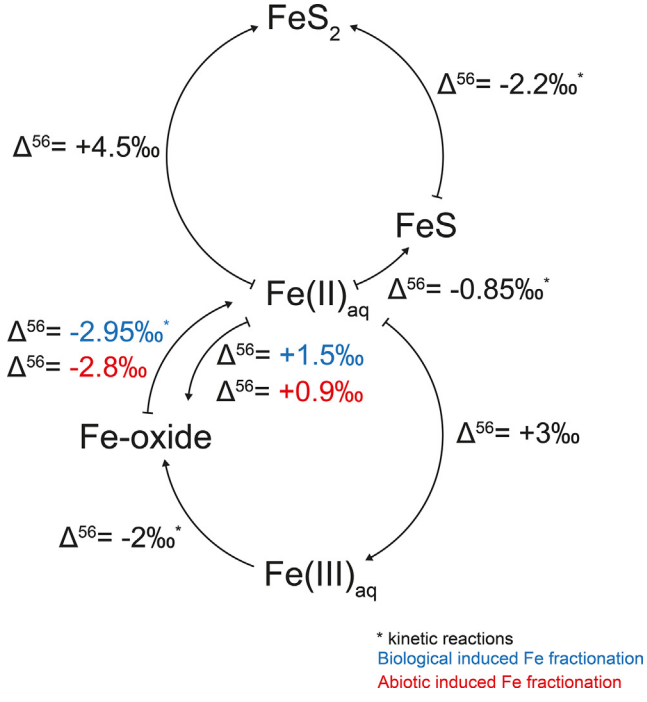

Fig. 8. Theoretical Fe isotopic fractionations between oxidized Fe species, ferrous Fe, monosulfide and pyrite. Data from Welch et al. (2003); Bullen et al. (2001); Croal et al. (2004); Guilbaud et al. (2011); Polyakov et al. (2007); Butler et al. (2005); Crosby et al. (2007). Blue and red colors indicate respectively Fe fractionations due to biological and abiotic reactions. (For interpretation of the references to colour in this figure legend, the reader is referred to the web version of this article.)

Please cite this article in press as: Decraene M. -N., et al. Intense biogeochemical iron cycling revealed in Neoarchean micropyrites from stromatolites. *Geochim. Cosmochim. Acta* (2021), https://doi.org/10.1016/j.gca.2021.07.020

the ~6‰ range in Fe isotope compositions measured in micropyrites by one or several of the fractionation processes described above.

4.2.2. Rayleigh distillation during precipitation of pyrites from monosulfides

Considering that the pyrites studied here have a synsedimentary origin, micropyrites Fe isotope signatures can result from a Rayleigh distillation process during conversion of pyrite precursors attending stromatolite growth or during early stages of diagenesis. Assuming Fe isotope composition of 0‰ for the overlying water column (Sharma et al., 2001; Beard et al., 2003; Severmann et al., 2004; Johnson et al., 2008), monosulfide pyrite precursor, most likely mackinawite, should in average carry a δ^{56}Fe value of about −0.85‰ (Butler et al., 2005). Using a fractionation factor between pyrite and mackinawite of $\Delta_{FeS2\text{-}FeS} = -2.2$‰ (Guilbaud et al., 2011), we can model the theoretical evolution of precipitated pyrite iron isotopes signature during a Rayleigh distillation process. Results of this isotopic evolution reported as a cumulative probability plot in Fig. 9 show a large isotopic range with values as high as 8‰. The observed range of values obtained in this study between −2.20‰ and +4.44‰ is completed for 98% of the Fe fraction precipitated as pyrites in the Rayleigh process. However, in the case of Rayleigh fractionation during the conversion of mackinawite to pyrite, a much higher abundance of isotopically light values would be expected, in contrast to what is observed in the micropyrites (Fig. 9). Additionally, a gradual increase of Fe isotopic compositions due to Rayleigh distillation may generate a specific spatial distribution, from low to progressively higher δ^{56}Fe values from the lamina to the sample scale. The random distribution of δ^{56}Fe values of the micropyrites within a single lamina (*e.g.*, GIS68.9; δ^{56}Fe from +0.08 ± 0.17‰ to +4.44 ± 0.16‰), which is observed in the whole sample, does not support the spatial distribution that might be expected during a Rayleigh distillation (Electronic Annex (EA); Fig. EA-8). Hence, we suggest that a single stage of pyrite precipitation associated with Rayleigh distillation is not supported here.

4.2.3. Variable pyrite precipitation rate

A recent study proposed that a combination of both kinetic and equilibrium isotopic effects could explain the whole Fe isotopic range in sedimentary pyrites recorded through geological history (Mansor and Fantle, 2019). Pyrites with positive δ^{56}Fe values can be formed under equilibrium considering a fractionation factor between pyrite and the initial $Fe(II)_{aq}$ of about +4.5‰ (Polyakov et al., 2007). Alternatively, pyrites with negative δ^{56}Fe values reflect kinetic effect between pyrite and mackinawite ($\Delta_{FeS2\text{-}FeS} = -2.2$‰, Guilbaud et al., 2011). Hence, to account for the large Fe isotopic range recorded in sedimentary pyrite, Mansor and Fantle (2019) proposed a variable expression of the kinetic (KIE) and equilibrium isotope effect (EIE) as a function of the rate of pyrite precipitation (RPP) and isotopic exchange between pyrite and $Fe(II)_{aq}$, the latter being controlled by the particle size and the concentrations of Fe(II) and H_2S in the system. For example, heavy Fe isotope pyrites are expected when EIE is expressed in association with low RPP. Consequently, pyrite showing δ^{56}Fe signatures close to 0‰ can reflect a growing influence of the KIE and an increase in RPP (Guilbaud et al., 2011; Mansor and Fantle, 2019). This hypothesis of a first order control on the δ^{56}Fe signal of pyrite precipitation on the long-time range (Guilbaud et al., 2011; Rolison et al., 2018) is further supported by the positive correlation

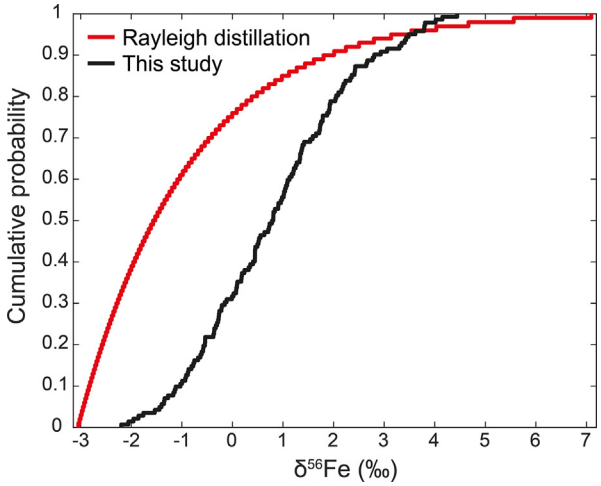

Fig. 9. Rayleigh distillation model. Cumulative function calculated for a near complete (98%) Rayleigh distillation (in red) using a fractionation factor of −2.2‰ between FeS_2 and FeS, and an initial $\delta^{56}Fe_{FeS}$ of −0.85‰ (Guilbaud et al, 2011; Butler et al, 2005). The black curve represents our dataset. δ^{56}Fe values for Rayleigh Distillation is given by $\delta^{56}Fe_{prod} = \alpha_{FeS2-FeS} * (\delta^{56}Fe_{res} + 1000) - 1000$ and $\delta^{56}Fe_{res} = (\delta^{56}Fe_{init} + 1000) * f^{(\alpha FeS2-FeS-1)} - 1000$, where "prod" refers to the product, "res" to the residue and f is the remaining fraction of reactant. The comparison suggests that a process of pyrite recrystallisation from monosulfides controlled by a Rayleigh distillation do not fit our measurements. (For interpretation of the references to colour in this figure legend, the reader is referred to the web version of this article.)

Please cite this article in press as: Decraene M. -N., et al. Intense biogeochemical iron cycling revealed in Neoarchean micropyrites from stromatolites. *Geochim. Cosmochim. Acta* (2021), https://doi.org/10.1016/j.gca.2021.07.020

revealed between δ^{56}Fe and δ^{34}S values recorded in sedimentary pyrites (Heard et al., 2020). At the scale of a single pyrite grain, we can assume that RPP is faster in the initial stage relative to the final stage of precipitation due to either $Fe(II)_{aq}$ and S pool availability or surface area to volume ratio variations. Accordingly, a single pyrite grain should show evolving isotope signal toward more positive δ^{56}Fe values from core to rim. Because of the size of the micropyrites and the low image resolution of the SIMS, profiles along pyrite grain were not completed here. Nonetheless, the exhaustive comparison between δ^{56}Fe values and the size of micropyrites does not show a specific trend (Fig. 5). The different concentrations of pyrites between the Type 1, 2 and 3 laminae may reflect variable Fe/S ratios or variable organic matter availability among these laminae, which should influence the RPP. Although micritic and organic-rich laminae include variable concentration of pyrites, comparison of Fe isotopic compositions between these two lamina types shows similar ranges, with δ^{56}Fe between −1.76‰ and +4.15‰ in the micritic laminae (Type 1) compared to −1.54‰ and +4.44‰ in the organic-rich laminae (Type 2). Comparable Fe isotopic ranges in both types of lamina suggests that the micropyrite Fe isotopic compositions are not controlled by the availability of organic matter between the lamina types. In a previous study focused on S isotope compositions of nanopyrites preserved in Type 2 organic-rich laminae, Marin-Carbonne et al. (2018) concluded that sulfate was a limiting reactant but may have been locally concentrated in micrometric scale niches. In our samples, the different laminae record variable amounts of detrital material that can account for varying Fe/S ratios at the micro-scale. The higher terrigenous fraction recognized in organic-rich laminae (see Section 4.1.2) should reflect a different Fe/H_2S ratio compare to micritic and fenestral laminae. However, micropyrites from organic-rich and micritic laminae seem to record random δ^{56}Fe ranges over a distance of one to several hundreds of microns (~4.2‰ in Fig. 10a, ~1.4‰ in Fig. 10b, ~2.7‰ in Fig. 10d and ~4‰ in Fig. 10e).

Progressive distillation of the ambient sulfate reservoir seems consistent with measurements performed in fenestral laminae, where we observed micropyrites in GIS68.1 distributed along a profile of ~400 µm displaying δ^{56}Fe values of +2.15‰, −0.92‰, −0.26‰, −0.88‰ and −1.27‰, respectively from the bottom to the top of the profile (Fig. 10c). This type of distribution is not systematic in fenestral laminae however, as shown by the randomly distributed δ^{56}Fe values (Fig. 10f). Therefore, this study does not fully support nor exclude that intra-facies δ^{56}Fe variability, recorded in micropyrites of the Tumbiana Formation, can reflect variation of the RPP during pyrite formation.

4.2.4. Sulfidation of highly-reactive Fe phases

The subsequent formation of monosulfide precursors (FeS) and pyrites can be promoted by sulfide mediated reductive dissolution of Fe(III)-oxides (Berner, 1984; Dos Santos Afonso and Stumm, 1992). The experimental

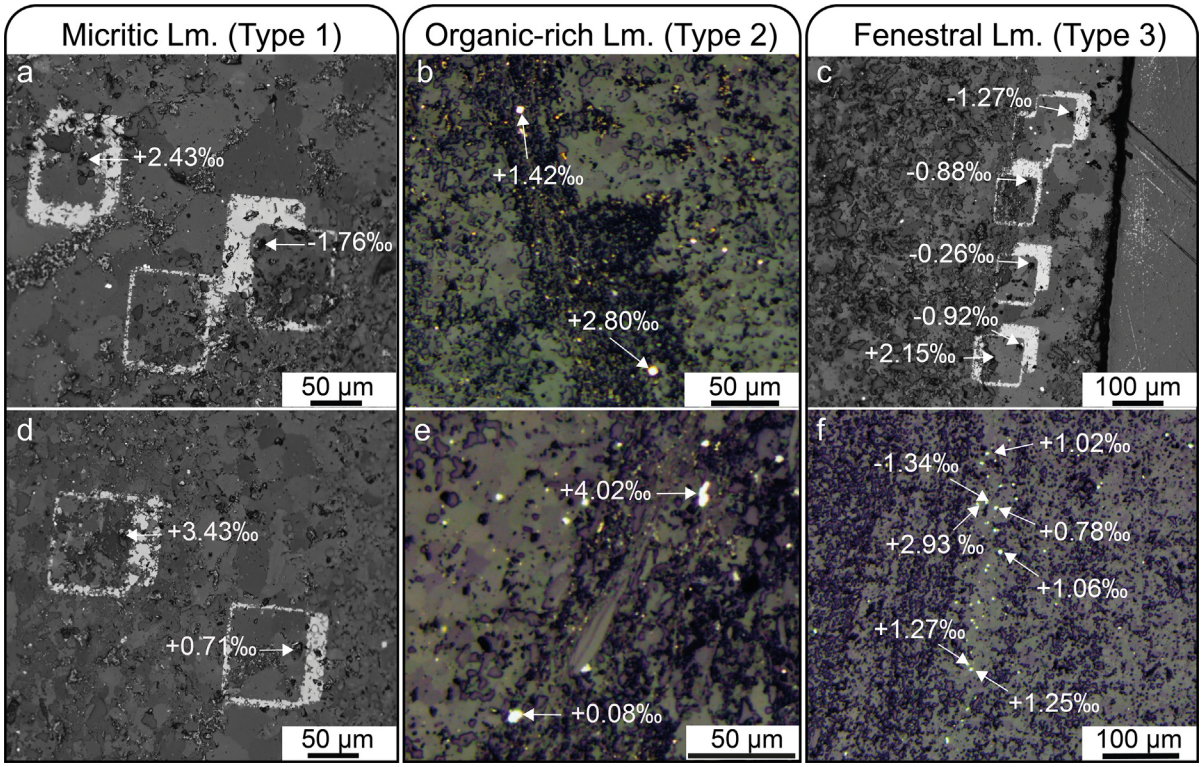

Fig. 10. SEM images of micropyrites and their corresponding δ^{56}Fe values in the different lamina types. (a) and (d) Fe isotopic compositions measured in micropyrites from micritic laminae (Type 1) in GIS68.1; b) and e) Fe isotopic compositions measured in micropyrites from organic-rich laminae (Type 2) in GIS68.9; c) and f) Fe isotopic compositions measured in micropyrites from fenestral laminae (Type 3) in GIS68.1 and GIS68.9.

Please cite this article in press as: Decraene M. -N., et al. Intense biogeochemical iron cycling revealed in Neoarchean micropyrites from stromatolites. *Geochim. Cosmochim. Acta* (2021), https://doi.org/10.1016/j.gca.2021.07.020

sulfidation of a variety of Fe(III)-bearing phases, such as ferrihydrite, goethite, hematite and lepidocrocite produces a significant Fe isotope fractionation of −0.85‰ ($\Delta^{56}Fe_{Fe2+aq\text{-}Fe(III)solid}$) and should be considered for cycling Fe in the sediment porewater (McAnena, 2011). If we cannot fully exclude abiotic sulfidation as an efficient reduction pathway of Fe(III)-oxides, this process alone is not likely to explain δ^{56}Fe values as low as −2.2‰.

4.2.5. Dissimilatory Iron Reduction (DIR)

A previous study has proposed that the Fe isotope composition of pyrites from the Tumbiana Formation can account for Dissimilatory Iron Reduction process (Yoshiya et al., 2012). Positive δ^{56}Fe values of pyrites can reflect the total reduction of preexisting Fe-oxides, while negative δ^{56}Fe values can be explained by partial reduction (Yoshiya et al., 2012). However, the recent discovery of negative Fe isotopic fractionation during abiotic Fe-oxides reduction that mimics DIR isotopic signatures (Frierdich et al., 2019) has changed the interpretation of the δ^{56}Fe signal. Knowing that abiotic Fe reduction can occur at similar rate than DIR in the presence of Fe-oxides and amorphous FeS (Mortimer et al., 2011), it seems difficult to firmly infer which one controlled pyrite precipitation and ensuing iron isotope signal. In the four analyzed samples, no Fe-oxide has been observed but the Fe speciation data support the presence of a non-negligible amount of Fe-oxides (between 90 ppm and 204 ppm, Table 1). The difference between partial and total iron reduction should therefore be due to organic matter availability. Indeed, the preservation of organic-matter in Type 2 laminae could be the result of partial reduction, whereas in Type 1 micritic laminae, the absence or discrete occurrence of organic matter, could reflect near-complete reduction. However, the rather comparable Fe isotopic ranges recorded in pyrites do not support the hypothesis of varying Fe reduction rate between Type 1 and 2 laminae. Thus, the preservation of organic-matter in Type 2 laminae is likely due to the ability of clays to adsorb organic-matter compared to micrite in Type 1 laminae.

Covariation between Fe and S isotopes could provide evidence for paired microbial Fe and sulfate reduction (Archer and Vance, 2006). A large S isotopic range measured in nanopyrites from organic-rich laminae (Type 2) has been previously interpreted as diagnostic for MSR (Marin-Carbonne et al., 2018). However, the Fe-S covariation proposed by Archer and Vance (2006) has not been tested at the micropyrite scale, although large isotopic ranges have been evidenced for both Fe (δ^{56}Fe from −1.5‰ to +4.4‰) and S (δ^{34}S from –33.7‰ to +50.4‰) for organic-rich laminae. The presence of iron enriched micrite (Fe > 0.5wt.%) in Type 1 laminae and magnetite, as indicated by iron speciation, can be either interpreted as a direct incorporaton of Fe(II) provided by the dissolution of mafic minerals, or as an end-product of DIR. Hence, if a microbial iron reduction seems plausible, it cannot solely explain the whole Fe isotopic distribution recorded in the four samples.

4.3. An emerging view of the biogeochemical Fe cycling recorded in Archean stromatolites

4.3.1. Pyrite Fe isotopes and microbial activity

In situ analyses applied to stromatolites from the Tumbiana Formation allowed the identification of S, C and Fe isotopic variations (Nishizawa et al., 2010; Yoshiya et al., 2012; Marin-Carbonne et al., 2018; Lepot et al., 2019) significantly different than those obtained so far by bulk-rock analyses (Thomazo et al., 2009; Czaja et al., 2010). These micro-scale heterogeneities in both organics and pyrites promote a microenvironmental, *i.e.* local, control on $\delta^{34}S_{py}$, $\delta^{13}C_{org}$ and $\delta^{56}Fe_{py}$ (Thomazo et al., 2009; Fike et al., 2015; Marin-Carbonne et al., 2018; Lepot et al., 2019). MSR has been previously called upon to explain S isotope heterogeneities and to be a major driver for micro- to nanometric pyrite precipitation on a local scale (Marin-Carbonne et al., 2018). Methanotroph metabolic activity, that can be aerobically mediated using oxygen (Hayes, 1994) or anaerobically (AOM for Anaerobic oxidation of Methane) using sulfates (Hinrichs, 2002), nitrates (Haroon et al., 2013) or even Fe-oxides (Beal et al., 2009), was likely active to create the large negative δ^{13}C excursion recorded in organic matter (Hayes, 1994; Thomazo et al., 2009; Lepot et al., 2019). C-isotope analyses of organic matter from another Tumbiana stromatolite samples (Lepot et al., 2019), equivalent to our Type 1 (micritic) laminae and Type 2 (organic-rich) laminae, revealed highly ^{13}C-depleted signatures as low as −58.8 ± 3.6‰ (SD) in micrite and −53.5 ± 1.8‰ (SD) in organic rich horizons. Extremely ^{13}C-depleted values of organic matter from micritic laminae associated with high abundance of organic sulfur have been interpreted as the result of sulfate-thriving AOM. The less negative $\delta^{13}C_{org}$ values recorded in organic matter from Type 2 laminae is interpreted to reflect a competition between sulfate and Fe-oxides during AOM (Lepot et al., 2019).

The three lamina types illustrate various concentration of organic-matter, terrigenous material and the effect of early diagenesis that can account for pyrite precipitation. The lower δ^{56}Fe values (δ^{56}Fe from −2.2‰ to +2.65‰) measured in micropyrites from fenestral laminae (Type 3), which are formed later compared to micritic and organic-rich laminae, can be related to the sparite filling that occured during early diagenesis. We can thus conclude that diagenetic processes affect the mean Fe isotopic composition recorded in micropyrites but the heterogeneity of δ^{56}Fe values is still preserved. The Fe isotopic record shows similar δ^{56}Fe variations and ranges between micritic and organic-rich laminae. Based on these two lamina types, the absence of variability rules out either a control of organic-matter, sulfate and Fe-oxides availability or a control of the biomineralization (higher in micritic laminae compared to organic-rich laminae) of the stromatolite on the Fe isotopic signatures. Therefore, the heterogeneity of δ^{56}Fe signatures seems to be primarily inherited from metabolic activities.

Please cite this article in press as: Decraene M. -N., et al. Intense biogeochemical iron cycling revealed in Neoarchean micropyrites from stromatolites. *Geochim. Cosmochim. Acta* (2021), https://doi.org/10.1016/j.gca.2021.07.020

4.3.2. A complex interplay of Fe redox reactions

Based on previous knowledge on microbial processes operating in the Tumbiana environment, we propose a multi-step model of iron cycling than can account for theδ^{56}Fe distribution attributed to the micropyrites. This model includes metabolisms previously proposed to be active in these stromatolites, such as MSR and AOM. While consistent with δ^{56}Fe measured in micropyrites and previous geochemical studies performed in the Tumbiana Formation, some uncertainties due to processes that could significantly contribute to Fe isotope signatures must be considered in the model. These include the influence of EIE/KIE, potential isotopic fractionation during the conversion of mackinawite into pyrites or isotopic variability inherited from the Fe source. The detrital Fe^{2+}_{aq} supplied by weathering of the mafic substrate (pathway 1, Fig. 11) was partially oxidized into Fe^{3+}, and precipitated as ferric oxide/hydroxides (pathway 2, Fig. 11). Whereas the question of the oxidant used for the $Fe(II)_{aq}$ oxidation remains open, Fe isotopic fractionations during partial oxidation mediated by O_2, anoxygenic photosynthesis or UV photooxidation are similar ranging from +0.9‰ to +1.5‰ (Bullen et al., 2001; Croal et al., 2004; Nie et al., 2017). We thus considered in the following section a mean isotopic fractionation between dissolved Fe^{2+} and Fe(III)-oxides/hydroxides $Fe(OH)_3$ of +1‰. Fe(III)-oxides/hydroxides are then used as electron acceptors during the microbial reduction mediated by DIR bacteria (1) (Czaja et al., 2010) or abiotically (2) (Mortimer et al., 2011) (pathway 3, Fig. 11).

$$4Fe(OH)_3 + CH_2O \rightarrow 4Fe^{2+} + HCO_3^- + 7OH^- + 3H_2O \quad (1)$$

$$2Fe(OH)_3 + FeS \rightarrow 3Fe^{2+} + S^0 + 6OH^- \quad (2)$$

On one hand, the biotic or abiotic Fe reduction is partial in order to generate Fe^{2+} depleted in ^{56}Fe with δ^{56}Fe values between −2‰ to −0.5‰. This ^{56}Fe-depleted iron source can be used in turn to react with reduced sulfur species (*e.g.*, H_2S, S_0) produced by MSR and hence precipitate successively as iron monosulfides and sedimentary pyrites (pathway 3a, Fig. 11). On the other hand, the partial reduction pathway allows the buildup of a residual Fe^{3+}-oxides/hydroxides pool which are experimentally shown to be

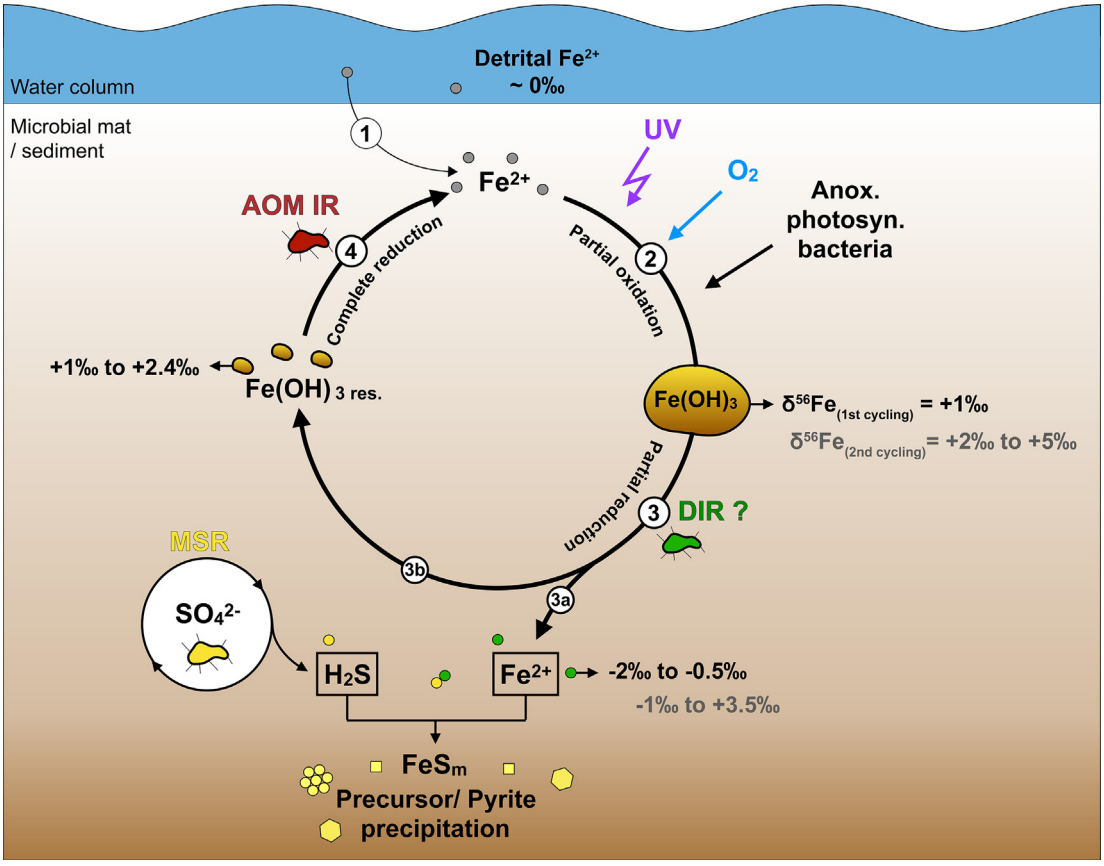

Fig. 11. Schematic view of microbial reactions discussed at local scale. Iron from water column is cycled several times by oxidation and reduction processes in the sediment. DIR: Dissimilatory Iron Reduction. MSR: Microbial Sulfate reduction. AOM IR: Anaerobic oxidation of methane coupled to iron reduction. Black numbers correspond to iron isotopic compositions of the different species at the first cycling. Grey numbers referred to iron isotopic compositions obtained after the second cycling. Probability density functions of the δ^{56}Fe distribution calculated for 4 cumulative Fe cycling (bin size of 0.1) and the comparison with probability density function of the δ^{56}Fe distribution of the 142 micropyrites are available in Electronic annex (Fig. EA-9). (For interpretation of the references to colour in this figure legend, the reader is referred to the web version of this article.)

Please cite this article in press as: Decraene M. -N., et al. Intense biogeochemical iron cycling revealed in Neoarchean micropyrites from stromatolites. *Geochim. Cosmochim. Acta* (2021), https://doi.org/10.1016/j.gca.2021.07.020

enriched in heavy iron isotope (Welch et al., 2003). The Fe isotopic compositions of the residual $Fe(OH)_3$ is estimated to range between +1‰ and +2.4‰ (pathway 3b, Fig. 11). This residual Fe(III)-oxides pool can later be fully converted back to Fe^{2+}, coupled for example with the activity of anaerobic methanotroph bacteria following the equation (3) (Czaja et al., 2010):

$$CH_4 + 8Fe(OH)_3 + 15H^+ \rightarrow HCO_3^- + 8Fe^{2+} + 21H_2O \quad (3)$$

The involvement of this step of complete reduction, possibly conducted by AOM-IR, allows to the preservation of the Fe isotopic range recorded by the residual Fe(III)-oxides. The conjoint activity of methanotrophs and potentially Fe reducing bacteria, leading to the formation of bicarbonate and ferrous iron, could participate to the precipitation of micrite observed in Type 2 laminae slightly enriched in iron. After reduction of Fe(III)-oxides into Fe^{2+}, possibly by methanotrophs, a re-cycling of this isotopically heavy dissolved Fe^{2+} could produced:

- δ^{56}Fe values of Fe-oxi/hydroxides from +2‰ to +5‰ after partial oxidation (pathway 2, 2nd cycling, Fig. 11).
- δ^{56}Fe values of Fe^{2+} from −1‰ to +3.5‰ after iron reduction (pathway 3a, 2nd cycling, Fig. 11). Isotopically heavier Fe^{2+} is available for pyrite precursor precipitations.

The model includes episodic supplies of detrital Fe^{2+} in the sediment pore water, likely generated by the weathering of mafic volcanoclastic substrate. The distribution of δ^{56}Fe values measured in Tumbiana micropyrites is best modeled after four successive cycles with a partial reduction rate of 30% (Electronic Annex (EA); Fig. EA-9), which is in the range of the reduction rate reported for Dissimilatory Iron Reduction in batch experiments (Benner et al., 2002; Hansel et al., 2004). Such an intensive Fe oxido-reduction iron cycling echoes Fe and S cryptic cycles, which can occur in modern stratified lacustrine environments (*e.g.*, Pavin lake, Cadagno lake; Berg et al., 2016; Berg et al., 2019) and oxygen minimum zone (*e.g.*, Chilean coast; Canfield et al., 2010; Teske, 2010). Independently of the Fe concentration of the water column, the subsequent Fe(II) oxidation and Fe-oxide reduction are the result of a prevalent microbial iron cycling in the water column chemocline (Berg et al., 2016; Berg et al., 2019). Although the origin of the oxidation is still questionable for Archean stromatolites such as those from the Tumbiana Formation, this study demonstrates the importance of local redox processes controlling the multiple step Fe cycling associated with coeval microbial metabolisms that promoted pyrite precipitation.

5. CONCLUSIONS

Iron isotope compositions of micropyrites from the 2.724 Ga Tumbiana Formation provide a unique view of the possible iron cycle during the Archean. Based on the study of stromatolite samples, four types of laminae have been evidenced: micritic (Type 1), organic-rich (Type 2), fenestral (Type 3) and coarse-grained (Type 4) laminae. These laminae reflect the different processes typically recognized in a stromatolite, such as carbonate precipitation (Type 1), terrigenous influence (Type 2), trapping and binding (Type 4) and cementation during early diagenesis (Type 3). Micropyrites recorded a local microenvironment and a limited impact of diagenesis. In addition to reflect a combined activity of AOM, MSR and possibly DIR, micropyrites recorded multiple stages of Fe oxidation and reduction. This study helps to better understand the iron isotopic signatures that result from multiple redox fluctuations in microbial mats. Therefore, stromatolites of the Tumbiana Formation can be considered to reflect a fossil microbial ecosystem that has recorded an exceptional diversity of microbial metabolisms. Future investigations should focus on the coupled Fe, S and C isotope evolution at the local scale in order to assess the effect of metabolism interactions on Fe isotope signatures.

Declaration of Competing Interest

The authors declare that they have no known competing financial interests or personal relationships that could have appeared to influence the work reported in this paper.

ACKNOWLEDGEMENTS

Johan Villeneuve and Nordine Bouden are thanked for their help during SIMS sessions. Colette Guilbaud is thanked for her help with sample preparation. Virgil Pasquier, Elias Bloch and Mathieu Gravey are thanked for fruitful discussions. Béatrice Luais is acknowledged for providing us standard material. This research was supported by the European Union's Horizon H2020 research and innovation program ERC (STROMATA, grant agreement 759289). Pascal Philippot acknowledges support from the São Paulo Research Foundation (FAPESP grant 2015/16235-2).

APPENDIX A. SUPPLEMENTARY DATA

Supplementary data to this article can be found online at https://doi.org/10.1016/j.gca.2021.07.020.

REFERENCES

Aller R. C., Mackin J. E. and Cox R. T. (1986) Diagenesis of Fe and S in Amazon inner shelf muds: apparent dominance of Fe reduction and implications for the genesis of ironstones. *Cont. Shelf Res.* **6**(1-2), 263–289.

Allwood A. C., Walter M. R., Kamber B. S., Marshall C. P. and Burch I. W. (2006) Stromatolite reef from the Early Archaean era of Australia. *Nature* **441**(7094), 714–718.

Aloisi G. (2008) The calcium carbonate saturation state in cyanobacterial mats throughout Earth's history. *Geochim. Cosmochim. Acta* **72**, 6037–6060.

Andres M. S. and Pamela Reid R. (2006) Growth morphologies of modern marine stromatolites: a case study from Highborne Cay Bahamas. *Sed. Geol.* **185**(3-4), 319–328.

Archer C. and Vance D. (2006) Coupled Fe and S isotope evidence for Archean microbial Fe(III) and sulfate reduction. *Geology* **34** (3), 153.

Arndt N., Nelson D., Compston W., Trendall A. and Thorne A. (1991) The age of the Fortescue Group, Hamersley Basin, Western Australia, from ion microprobe zircon U-Pb results. *Aust. J. Earth Sci.* **38**, 261–281.

Arp G., Reimer A. and Reitner J. (2003) Microbialite formation in seawater of increased alkalinity, Satonda Crater Lake. *Indonesia. J. Sed. Res.* **73**, 105–127.

Awramik S., Margulis L. and Barghoorn E. (1976) Evolutionary processes in the formation of stromatolites. *Devel. Sed.*, 149–162.

Awramik S. M. (2006) Palaeontology: respect for stromatolites. *Nature* **441**(7094), 700–701.

Awramik S. M. and Buchheim H. P. (2009) A giant, Late Archean lake system: The Meentheena Member (Tumbiana Formation; Fortescue Group), Western Australia. *Precambrian Res.* **174**(3-4), 215–240.

Awramik S. M. and Grey K. (2005) Stromatolites: biogenicity, biosignatures, and bioconfusion. *Astro. Planet. Miss.* **5906**, 59060P.

Beal E. J., House C. H. and Orphan V. J. (2009) Manganese-and iron-dependent marine methane oxidation. *Science* **325**(5937), 184–187.

Beard B. L., Johnson C. M., Von Damm K. L. and Poulson R. L. (2003) Iron isotope constraints on Fe cycling and mass balance in oxygenated Earth oceans. *Geology* **31**(7), 629.

Benner S. G., Hansel C. M., Wielinga B. W., Barber T. M. and Fendorf S. (2002) Reductive dissolution and biomineralization of iron hydroxide under dynamic flow conditions. *Envir. Sci. Tech.* **36**(8), 1705–1711.

Berner R. A. (1984) Sedimentary pyrite formation: an update. *Geochim. Cosmochim. Acta* **48**, 605–615.

Berg J. S., Michellod D., Pjevac P., Martinez-Perez C., Buckner C. R., Hach P. F., Schubert C. J., Milucka J. and Kuypers M. M. (2016) Intensive cryptic microbial iron cycling in the low iron water column of the meromictic Lake Cadagno. *Environ. Microbiol.* **18**, 5288–5302.

Berg J. S., Jézéquel D., Duverger A., Lamy D., Laberty-Robert C., Miot J. and Senko J. M. (2019) Microbial diversity involved in iron and cryptic sulfur cycling in the ferruginous, low-sulfate waters of Lake Pavin. *PLoS One* **14**(2), e0212787.

Blake T. S. (1993) Late Archaean crustal extension, sedimentary basin formation, flood basalt volcanism and continental rifting: the Nullagine and Mount Jope Supersequences, Western Australia. *Precambrian Res.* **60**(1-4), 185–241.

Blake T. S. and Barley M. E. (1992) Tectonic evolution of the Late Archaean to Early Proterozoic Mount Bruce Megasequence Set, Western Australia. *Tectonics* **11**(6), 1415–1425.

Blake T. S., Buick R., Brown S. J. A. and Barley M. E. (2004) Geochronology of a Late Archaean flood basalt province in the Pilbara Craton, Australia: constraints on basin evolution, volcanic and sedimentary accumulation, and continental drift rates. *Precambrian Res.* **133**(3-4), 143–173.

Bolhar R. and Vankranendonk M. (2007) A non-marine depositional setting for the northern Fortescue Group, Pilbara Craton, inferred from trace element geochemistry of stromatolitic carbonates. *Precambrian Res.* **155**(3-4), 229–250.

Bouton A., Vennin E., Pace A., Bourillot R., Dupraz C., Thomazo C., Brayard A., Désaubliaux G., Visscher P. T. and Lokier S. (2016) External controls on the distribution, fabrics and mineralization of modern microbial mats in a coastal hypersaline lagoon, Cayo Coco (Cuba). *Sedimentology* **63**(4), 972–1016.

Bouton A., Vennin E., Amiotte-Suchet P., Thomazo C., Sizun J.-P., Virgone A., Gaucher E. C. and Visscher P. T. (2020) Prediction of the calcium carbonate budget in a sedimentary basin: A "source-to-sink" approach applied to Great Salt Lake, Utah, USA. *Basin Res.* **32**(5), 1005–1034.

Bowlin E. M., Klaus J. S., Foster J. S., Andres M. S., Custals L. and Reid R. P. (2012) Environmental controls on microbial community cycling in modern marine stromatolites. *Sediment. Geol.* **263-264**, 45–55.

Brantley S. L., Liermann L. and Bullen T. D. (2001) Fractionation of Fe isotopes by soil microbes and organic acids. *Geology* **29**(6), 535.

Brantley S. L., Liermann L. J., Guynn R. L., Anbar A., Icopini G. A. and Barling J. (2004) Fe isotopic fractionation during mineral dissolution with and without bacteria. *Geochim. Cosmochim. Acta* **68**, 3189–3204.

Buick R. (1992) The Antiquity of Oxygenic Photosynthesis - Evidence from Stromatolites in Sulfate-Deficient Archean Lakes. *Science* **255**, 74–77.

Bullen T. D., White A. F., Childs C. W., Vivit D. V. and Schulz M. S. (2001) Demonstration of significant abiotic iron isotope fractionation in nature. *Geology* **29**(8), 699.

Butler I. B., Archer C., Vance D., Oldroyd A. and Rickard D. (2005) Fe isotope fractionation on FeS formation in ambient aqueous solution. *Earth Planet. Sci. Lett.* **236**, 430–442.

Canfield D. E., Raiswell R. and Bottrell S. (1992) The Reactivity of Sedimentary Iron Minerals toward Sulfide. *Am. J. Sci.* **292**, 659–683.

Canfield D. E., Raiswell R., Westrich J. T., Reaves C. M. and Berner R. A. (1986) The Use of Chromium Reduction in the Analysis of Reduced Inorganic Sulfur in Sediments and Shales. *Chem. Geol.* **54**, 149–155.

Canfield D. E., Stewart F. J., Thamdrup B., De Brabandere L., Dalsgaard T., Delong E. F., Revsbech N. P. and Ulloa O. (2010) A cryptic sulfur cycle in oxygen-minimum–zone waters off the Chilean coast. *Science* **330**(6009), 1375–1378.

Chapman J. B., Weiss D. J., Shan Y. and Lemburger M. (2009) Iron isotope fractionation during leaching of granite and basalt by hydrochloric and oxalic acids. *Geochim. Cosmochim. Acta* **73**, 1312–1324.

Choquette P. W. and Pray L. C. (1970) Geologic nomenclature and classification of porosity in sedimentary carbonates. *AAPG Bull.* **54**, 207–250.

Coffey J. M., Flannery D. T., Walter M. R. and George S. C. (2013) Sedimentology, stratigraphy and geochemistry of a stromatolite biofacies in the 2.72 Ga Tumbiana Formation, Fortescue Group Western Australia. *Precambrian Res.* **236**, 282–296.

Croal L. R., Johnson C. M., Beard B. L. and Newman D. K. (2004) Iron isotope fractionation by Fe(II)-oxidizing photoautotrophic bacteria. *Geochim. Cosmochim. Acta* **68**, 1227–1242.

Crosby H. A., Johnson C. M., Roden E. E. and Beard B. L. (2005) Coupled Fe(II)-Fe(III) electron and atom exchange as a mechanism for Fe isotope fractionation during dissimilatory iron oxide reduction. *Environ. Sci. Technol.* **39**(17), 6698–6704.

Crosby H. A., Roden E. E., Johnson C. M. and Beard B. L. (2007) The mechanisms of iron isotope fractionation produced during dissimilatory Fe(III) reduction by Shewanella putrefaciens and Geobacter sulfurreducens. *Geobiology* **5**(2), 169–189.

Crowe S. A., Paris G., Katsev S., Jones C., Kim S.-T., Zerkle A. L., Nomosatryo S., Fowle D. A., Adkins J. F., Sessions A. L., Farquhar J. and Canfield D. E. (2014) Sulfate was a trace constituent of Archean seawater. *Science* **346**(6210), 735–739.

Czaja A. D., Johnson C. M., Beard B. L., Eigenbrode J. L., Freeman K. H. and Yamaguchi K. E. (2010) Iron and carbon isotope evidence for ecosystem and environmental diversity in the similar to 2.7 to 2.5 Ga Hamersley Province Western Australia. *Earth Planet. Sci. Lett.* **292**, 170–180.

Please cite this article in press as: Decraene M. -N., et al. Intense biogeochemical iron cycling revealed in Neoarchean micropyrites from stromatolites. *Geochim. Cosmochim. Acta* (2021), https://doi.org/10.1016/j.gca.2021.07.020

Dauphas N., John S. G. and Rouxel O. (2017) Iron Isotope Systematics. *Rev. Mineral Geochem.* **82**(1), 415–510.

Decraene M. N., Marin-Carbonne J., Bouvier A. S., Villeneuve J., Bouden N., Luais B. and Deloule E. (2021) High-spatial-resolution measurements of iron isotopes in pyrites by secondary ion mass spectrometry using the new Hyperion-II radio-frequency plasma source. *Rapid Commun. Mass Spectrom.* **35** e8986.

Dos Santos Afonso M. and Stumm W. (1992) Reductive dissolution of iron (III)(hydr) oxides by hydrogen sulfide. *Langmuir* **8** (6), 1671–1675.

Dupraz C., Reid R. P., Braissant O., Decho A. W., Norman R. S. and Visscher P. T. (2009) Processes of carbonate precipitation in modern microbial mats. *Earth Sci. Rev.* **96**, 141–162.

Eigenbrode J. L. and Freeman K. H. (2006) Late Archean rise of aerobic microbial ecosystems. *Proc. Natl. Acad. Sci. USA* **103** (43), 15759–15764.

Fike D. A., Bradley A. S. and Rose C. V. (2015) Rethinking the ancient sulfur cycle. *Annu. Rev. Earth Pl. Sc.* **43**, 593–622.

Flament N., Rey P. F., Coltice N., Dromart G. and Olivier N. (2011) Lower crustal flow kept Archean continental flood basalts at sea level. *Geology* **39**, 1159–1162.

Flannery D. T., Van Kranendonk M. J., Mazumder R. and Walter M. R. (2014) The ca 2.74 Ga Mopoke Member, Kylena Formation: a marine incursion into the northern Fortescue Group? *Aust. J. Earth Sci.* **61**, 1095–1108.

Flannery D. T. and Walter M. R. (2012) Archean tufted microbial mats and the Great Oxidation Event: new insights into an ancient problem. *Aust. J. Earth Sci.* **59**(1), 1–11.

Frierdich A. J., Nebel O., Beard B. L. and Johnson C. M. (2019) Iron isotope exchange and fractionation between hematite (alpha-Fe_2O_3) a and aqueous Fe(II): A combined three-isotope and reversal-approach to equilibrium study. *Geochim. Cosmochim. Acta* **245**, 207–221.

Guilbaud R., Butler I. B. and Ellam R. M. (2011) Abiotic pyrite formation produces a large Fe isotope fractionation. *Science* **332**(6037), 1548–1551.

Hansel C. M., Benner S. G., Nico P. and Fendorf S. (2004) Structural constraints of ferric (hydr) oxides on dissimilatory iron reduction and the fate of Fe (II). *Geochim. Cosmochim. Acta* **68**, 3217–3229.

Haroon M. F., Hu S., Shi Y., Imelfort M., Keller J., Hugenholtz P., Yuan Z. and Tyson G. W. (2013) Anaerobic oxidation of methane coupled to nitrate reduction in a novel archaeal lineage. *Nature* **500**(7464), 567–570.

Hayes J. (1994) *Global methanotrophy at the Archean-Proterozoic transition*. Columbia University Press, New York, pp. 220–235.

Heard A. W., Dauphas N., Guilbaud R., Rouxel O. J., Butler I. B., Nie N. X. and Bekker A. (2020) Triple iron isotope constraints on the role of ocean iron sinks in early atmospheric oxygenation. *Science* **370**(6515), 446–449.

Hinrichs K. U. (2002) Microbial fixation of methane carbon at 2.7 Ga: Was an anaerobic mechanism possible? *Geochem. Geophy. Geosy.* **3**, 1–10.

Jahnert R. J., Collins L. B. and Ariztegui D. (2013) Controls on microbial activity and tidal flat evolution in Shark Bay, Western Australia. *Sedimentology* **60**(4), 1071–1099.

Jardine P., McCarthy J. and Weber N. (1989) Mechanisms of dissolved organic carbon adsorption on soil. *Soil Sci. Soc. Am. J.* **53**, 1378–1385.

Johnson C. M., Roden E. E., Welch S. A. and Beard B. L. (2005) Experimental constraints on Fe isotope fractionation during magnetite and Fe carbonate formation coupled to dissimilatory hydrous ferric oxide reduction. *Geochim. Cosmochim. Acta* **69**, 963–993.

Johnson C. M., Beard B. L. and Roden E. E. (2008) The iron isotope fingerprints of redox and biogeochemical cycling in the modern and ancient Earth. *Annu. Rev. Earth Pl. Sc.* **36**, 457–493.

Johnston D. T. (2011) Multiple sulfur isotopes and the evolution of Earth's surface sulfur cycle. *Earth Sci. Rev.* **106**, 161–183.

Kiczka M., Wiederhold J. G., Frommer J., Kraemer S. M., Bourdon B. and Kretzschmar R. (2010) Iron isotope fractionation during proton-and ligand-promoted dissolution of primary phyllosilicates. *Geochim. Cosmochim. Acta* **74**, 3112–3128.

Lepot K., Benzerara K., Brown G. E. and Philippot P. (2008) Microbially influenced formation of 2,724-million-year-old stromatolites. *Nat. Geosci.* **1**, 118–121.

Lepot K., Benzerara K., Rividi N., Cotte M., Brown G. E. and Philippot P. (2009) Organic matter heterogeneities in 2.72 Ga stromatolites: Alteration versus preservation by sulfur incorporation. *Geochim. Cosmochim. Acta* **73**, 6579–6599.

Lepot K., Williford K. H., Philippot P., Thomazo C., Ushikubo T., Kitajima K., Mostefaoui S. and Valley J. W. (2019) Extreme 13C-depletions and organic sulfur content argue for S-fueled anaerobic methane oxidation in 2.72 Ga old stromatolites. *Geochim. Cosmochim. Acta* **244**, 522–547.

Liu M.-C., McKeegan K. D., Harrison T. M., Jarzebinski G. and Vltava L. (2018) The Hyperion-II radio-frequency oxygen ion source on the UCLA ims1290 ion microprobe: Beam characterization and applications in geochemistry and cosmochemistry. *Int. J. Mass Spectrom.* **424**, 1–9.

Lyons T. W. and Severmann S. (2006) A critical look at iron paleoredox proxies: New insights from modern euxinic marine basins. *Geochim. Cosmochim. Acta* **70**(23), 5698–5722.

Mansor M. and Fantle M. S. (2019) A novel framework for interpreting pyrite-based Fe isotope records of the past. *Geochim. Cosmochim. Acta* **253**, 39–62.

Marin-Carbonne J., Chaussidon M. and Robert F. (2012) Micrometer-scale chemical and isotopic criteria (O and Si) on the origin and history of Precambrian cherts: Implications for paleo-temperature reconstructions. *Geochim. Cosmochim. Acta* **92**, 129–147.

Marin-Carbonne J., Remusat L., Sforna M. C., Thomazo C., Cartigny P. and Philippot P. (2018) Sulfur isotope's signal of nanopyrites enclosed in 2.7 Ga stromatolitic organic remains reveal microbial sulfate reduction. *Geobiology* **16**(2), 121–138.

Marin-Carbonne J., Rollion-Bard C., Bekker A., Rouxel O., Agangi A., Cavalazzi B., Wohlgemuth-Ueberwasser C. C., Hofmann A. and McKeegan K. D. (2014) Coupled Fe and S isotope variations in pyrite nodules from Archean shale. *Earth Planet. Sci. Lett.* **392**, 67–79.

Marin-Carbonne J., Rollion-Bard C. and Luais B. (2011) In-situ measurements of iron isotopes by SIMS: MC-ICP-MS intercalibration and application to a magnetite crystal from the Gunflint chert. *Chem. Geol.* **285**(1-4), 50–61.

Mata S. A., Harwood C. L., Corsetti F. A., Stork N. J., Eilers K., Berelson W. M. and Spear J. R. (2012) Influence of gas production and filament orientation on stromatolite microfabric. *Palaios* **27**(4), 206–219.

McAnena A. (2011) The reactivity and isotopic fractionation of Fe-bearing minerals during sulfidation: an experimental approach. *Newcastle University*.

Mortimer R. J. G., Galsworthy A. M. J., Bottrell S. H., Wilmot L. E. and Newton R. J. (2011) Experimental evidence for rapid biotic and abiotic reduction of Fe (III) at low temperatures in salt marsh sediments: a possible mechanism for formation of modern sedimentary siderite concretions. *Sedimentology* **58**, 1514–1529.

Nie N. X., Dauphas N. and Greenwood R. C. (2017) Iron and oxygen isotope fractionation during iron UV photo-oxidation:

Please cite this article in press as: Decraene M. -N., et al. Intense biogeochemical iron cycling revealed in Neoarchean micropyrites from stromatolites. *Geochim. Cosmochim. Acta* (2021), https://doi.org/10.1016/j.gca.2021.07.020

Implications for early Earth and Mars. *Earth Planet. Sci. Lett.* **458**, 179–191.

Nishizawa M., Yamamoto H., Ueno Y., Tsuruoka S., Shibuya T., Sawaki Y., Yamamoto S., Kon Y., Kitajima K., Komiya T., Maruyama S. and Hirata T. (2010) Grain-scale iron isotopic distribution of pyrite from Precambrian shallow marine carbonate revealed by a femtosecond laser ablation multicollector ICP-MS technique: Possible proxy for the redox state of ancient seawater. *Geochim. Cosmochim. Acta* **74**, 2760–2778.

Philippot P., Van Kranendonk M., Van Zuilen M., Lepot K., Rividi N., Teitler Y., Thomazo C., Blanc-Valleron M.-M., Rouchy J.-M., Grosch E. and de Wit M. (2009) Early traces of life investigations in drilling Archean hydrothermal and sedimentary rocks of the Pilbara Craton, Western Australia and Barberton Greenstone Belt, South Africa. *Cr Palevol* **8**(7), 649–663.

Planavsky N. and Grey K. (2008) Stromatolite branching in the Neoproterozoic of the Centralian Superbasin, Australia: an investigation into sedimentary and microbial control of stromatolite morphology. *Geobiology* **6**, 33–45.

Polyakov V. B., Clayton R. N., Horita J. and Mineev S. D. (2007) Equilibrium iron isotope fractionation factors of minerals: reevaluation from the data of nuclear inelastic resonant X-ray scattering and Mössbauer spectroscopy. *Geochim. Cosmochim. Acta* **71**(15), 3833–3846.

Poulton S. W. and Canfield D. E. (2005) Development of a sequential extraction procedure for iron: implications for iron partitioning in continentally derived particulates. *Chem. Geol.* **214**(3-4), 209–221.

Raiswell R. and Canfield D. E. (1998) Sources of iron for pyrite formation in marine sediments. *Am. J. Sci.* **298**, 219–245.

Reid R. P., Visscher P. T., Decho A. W., Stolz J. F., Bebout B. M., Dupraz C., Macintyre I. G., Paerl H. W., Pinckney J. L., Prufert-Bebout L., Steppe T. F. and DesMarais D. J. (2000) The role of microbes in accretion, lamination and early lithification of modern marine stromatolites. *Nature* **406** (6799), 989–992.

Reuschel M., Melezhik V. A. and Strauss H. (2012) Sulfur isotopic trends and iron speciation from the c. 2.0 Ga Pilgujarvi Sedimentary Formation, NW Russia. *Precambrian Res.* **196**, 193–203.

Rickard D., Mussmann M. and Steadman J. A. (2017) Sedimentary sulfides. *Elements* **13**(2), 117–122.

Rolison J. M., Stirling C. H., Middag R., Gault-Ringold M., George E. and Rijkenberg M. J. A. (2018) Iron isotope fractionation during pyrite formation in a sulfidic Precambrian ocean analogue. *Earth Planet. Sci. Lett.* **488**, 1–13.

Sakurai R., Ito M., Ueno Y., Kitajima K. and Maruyama S. (2005) Facies architecture and sequence-stratigraphic features of the Tumbiana Formation in the Pilbara Craton, northwestern Australia: Implications for depositional environments of oxygenic stromatolites during the Late Archean. *Precambrian Res.* **138**(3-4), 255–273.

Sauvage L., Riquier L., Thomazo C., Baudin F. and Martinez M. (2013) The late Hauterivian Faraoni "Oceanic Anoxic Event" at Rio Argos (southern Spain): An assessment on the level of oxygen depletion. *Chem. Geol.* **340**, 77–90.

Schidlowski M. (1982) Content and isotopic composition of reduced carbon in sediments. *Mineral Dep. Evol. Bio. Springer*, 103–122.

Schopf J. W., Kudryavtsev A. B., Czaja A. D. and Tripathi A. B. (2007) Evidence of Archean life: stromatolites and microfossils. *Precambrian Res.* **158**(3-4), 141–155.

Severmann S., Johnson C. M., Beard B. L., German C. R., Edmonds H. N., Chiba H. and Green D. R. H. (2004) The effect of plume processes on the Fe isotope composition of hydrothermally derived Fe in the deep ocean as inferred from the Rainbow vent site, Mid-Atlantic Ridge, 36 degrees 14' N. *Earth Planet. Sci. Lett.* **225**, 63–76.

Sforna M. C., Philippot P., Somogyi A., van Zuilen M. A., Medjoubi K., Schoepp-Cothenet B., Nitschke W. and Visscher P. T. (2014) Evidence for arsenic metabolism and cycling by microorganisms 2.7 billion years ago. *Nat. Geosci.* **7**, 811–815.

Shahar A., Young E. D. and Manning C. E. (2008) Equilibrium high-temperature Fe isotope fractionation between fayalite and magnetite: an experimental calibration. *Earth Planet. Sci. Lett.* **268**, 330–338.

Sharma M., Polizzotto M. and Anbar A. D. (2001) Iron isotopes in hot springs along the Juan de Fuca Ridge. *Earth Planet. Sci. Lett.* **194**, 39–51.

Sim M. S., Bosak T. and Ono S. (2011) Large sulfur isotope fractionation does not require disproportionation. *Science* **333** (6038), 74–77.

Slotznick S. P. and Fischer W. W. (2016) Examining Archean methanotrophy. *Earth Planet. Sci. Lett.* **441**, 52–59.

Sossi P. A., Foden J. D. and Halverson G. P. (2012) Redox-controlled iron isotope fractionation during magmatic differentiation: an example from the Red Hill intrusion, S Tasmania. *Contribut. Mineral. Petrol.* **164**(5), 757–772.

Stüeken E. E., Buick R., Anderson R. E., Baross J. A., Planavsky N. J. and Lyons T. W. (2017) Environmental niches and metabolic diversity in Neoarchean lakes. *Geobiology* **15**(6), 767–783.

Stüeken E. E., Buick R., Bekker A., Catling D., Foriel J., Guy B. M., Kah L. C., Machel H. G., Montañez I. P. and Poulton S. W. (2015a) The evolution of the global selenium cycle: Secular trends in Se isotopes and abundances. *Geochim. Cosmochim. Acta* **162**, 109–125.

Stüeken E. E., Buick R. and Schauer A. J. (2015b) Nitrogen isotope evidence for alkaline lakes on late Archean continents. *Earth Planet. Sci. Lett.* **411**, 1–10.

Sugisaki R. (1978) Chemical composition of argillaceous sediments on the Pacific margin of southwest Japan.

Sugitani K., Horiuchi Y., Adachi M. and Sugisaki R. (1996) Anomalously low Al2O3/TiO2 values for Archean cherts from the Pilbara block, western Australia - Possible evidence for extensive chemical weathering on the early earth. *Precambrian Res.* **80**, 49–76.

Tebbutt G. E., Conley C. D. and Boyd D. W. (1965) Lithogenesis of a distinctive carbonate rock fabric. *Rock. Mount. Geol.* **4**, 1–13.

Teng F.-Z., Dauphas N., Helz R. T., Gao S. and Huang S. (2011) Diffusion-driven magnesium and iron isotope fractionation in Hawaiian olivine. *Earth Planet. Sci. Lett.* **308**, 317–324.

Teske A. (2010) Cryptic links in the ocean. *Science* **330**(6009), 1326–1327.

Thomazo C., Ader M., Farquhar J. and Philippot P. (2007) Multiple Sulfur and Carbon isotopic chemiostratigraphy of the 2.73 Ga carbonated Tumbiana formation, new insights for the Fortescue excursion. *Geochim. Cosmochim. Acta* **71**, A1019.

Thomazo C., Ader M., Farquhar J. and Philippot P. (2009) Methanotrophs regulated atmospheric sulfur isotope anomalies during the Mesoarchean (Tumbiana Formation, Western Australia). *Earth Planet. Sci. Lett.* **279**, 65–75.

Thomazo C., Oeser M., Strauss H. and Philippot P. (2010) Late Archean oceanic redox fluctuations revealed by iron speciation in the 2.73Ga old Tumbiana Formation. *Geochim. Cosmochim. Acta* **74**, A1042.

Thomazo C., Ader M. and Philippot P. (2011) Extreme 15N-enrichments in 2.72-Gyr-old sediments: evidence for a turning point in the nitrogen cycle. *Geobiology* **9**, 107–120.

Please cite this article in press as: Decraene M. -N., et al. Intense biogeochemical iron cycling revealed in Neoarchean micropyrites from stromatolites. *Geochim. Cosmochim. Acta* (2021), https://doi.org/10.1016/j.gca.2021.07.020

Thorne A. and Trendall A. F. (2001) Geology of the Fortescue Group, Pilbara Craton, Western Australia. *Bull. Geol. Surv. West. Aust.* **144**, 1–249.

Visscher P. T., Reid R. P., Bebout B. M., Hoeft S. E., Macintyre I. G. and Thompson J. A. (1998) Formation of lithified micritic laminae in modern marine stromatolites (Bahamas); the role of sulfur cycling. *Am. Mineral.* **83**(11-12 Part 2), 1482–1493.

Welch S. A., Beard B. L., Johnson C. M. and Braterman P. S. (2003) Kinetic and equilibrium Fe isotope fractionation between aqueous Fe(II) and Fe(III). *Geochim. Cosmochim. Acta* **67**, 4231–4250.

White A., Legras M., Smith R. and Nadoll P. (2014) Deformation-driven, regional-scale metasomatism in the Hamersley Basin, Western Australia. *J. Metam. Geol.* **32**, 417–433.

Whitehouse M. J. and Fedo C. M. (2007) Microscale heterogeneity of Fe isotopes in > 3.71 Ga banded iron formation from the Isua Greenstone Belt Southwest Greenland. *Geology* **35**, 719–722.

Wiesli R. A., Beard B. L. and Johnson C. M. (2004) Experimental determination of Fe isotope fractionation between aqueous Fe (II), siderite and "green rust" in abiotic systems. *Chem. Geol.* **211**, 343–362.

Williford K. H., Ushikubo T., Lepot K., Kitajima K., Hallmann C., Spicuzza M. J., Kozdon R., Eigenbrode J. L., Summons R. E. and Valley J. W. (2016) Carbon and sulfur isotopic signatures of ancient life and environment at the microbial scale: Neoarchean shales and carbonates. *Geobiology* **14**(2), 105–128.

Wintsch R. P. and Kvale C. M. (1994) Differential Mobility of Elements in Burial Diagenesis of Siliciclastic Rocks. *J. Sediment. Res. A* **64**, 349–361.

Yoshiya K., Nishizawa M., Sawaki Y., Ueno Y., Komiya T., Yamada K., Yoshida N., Hirata T., Wada H. and Maruyama S. (2012) In situ iron isotope analyses of pyrite and organic carbon isotope ratios in the Fortescue Group: Metabolic variations of a Late Archean ecosystem. *Precambrian Res.* **212-213**, 169–193.

Associate editor: Aubrey Zerkle